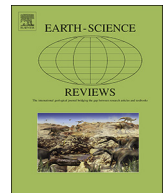




Contents lists available at ScienceDirect

## Earth-Science Reviews

journal homepage: [www.elsevier.com/locate/earscirev](http://www.elsevier.com/locate/earscirev)

## Tidal modulation of plate motions

Davide Zaccagnino<sup>a</sup>, Francesco Vespe<sup>b</sup>, Carlo Doglioni<sup>c,d,\*</sup><sup>a</sup> Dipartimento di Fisica, Università Sapienza di Roma, Italy<sup>b</sup> Agenzia Spaziale Italiana, Matera, Italy<sup>c</sup> Dipartimento di Scienze della Terra, Università Sapienza di Roma, Italy<sup>d</sup> Istituto Nazionale di Geofisica e Vulcanologia, Roma, Italy

## ARTICLE INFO

## Keywords:

Plate tectonics

Driving forces

Body tide horizontal component

## ABSTRACT

While mantle convection is a fundamental ingredient of geodynamics, the driving mechanism of plate tectonics remains elusive. Are plates driven only from the thermal cooling of the mantle or are there further astronomical forces acting on them? GPS measurements are now accurate enough that, on long baselines, both secular plate motions and periodic tidal displacements are visible. The now > 20 year-long space geodesy record of plate motions allows a more accurate analysis of the contribution of the horizontal component of the body tide in shifting the lithosphere. We review the data and show that lithospheric plates retain a non-zero horizontal component of the solid Earth tidal waves and their speed correlates with tidal harmonics. High-frequency semidiurnal Earth's tides are likely contributing to plate motions, but their residuals are still within the error of the present accuracy of GNSS data. The low-frequency body tides rather show horizontal residuals equal to the relative motion among plates, proving the astronomical input on plate dynamics. Plates move faster with nutation cyclicity of 8.8 and 18.6 years that correlate to lunar apsidal migration and nodal precession. The high-frequency body tides are mostly buffered by the high viscosity of the lithosphere and the underlying mantle, whereas low-frequency horizontal tidal oscillations are compatible with the relaxation time of the low-velocity zone and can westerly drag the lithosphere over the asthenospheric mantle. Variable angular velocities among plates are controlled by the viscosity anisotropies in the decoupling layer within the low-velocity zone. Tidal oscillations also correlate with the seismic release.

## 1. Introduction

One of the most intriguing frontiers in geodynamic concerns the causes and the driving mechanisms of plate motions, which are fundamental for the understanding of all the geological phenomena we observe on our planet (Vidale et al., 1998, Ryan et al., 2009). Some inconsistencies between theoretical models and experimental data question the origin, layering, and vigour of mantle convection. Among these are the subadiabaticity of the lower mantle (Anderson and Natland, 2014), the estimation of the density gradient between lithosphere and mantle to sink plates along subduction zones (Afonso et al., 2007; Doglioni and Panza, 2015). Nevertheless, mantle convection occurs and is a basic phenomenon of plate tectonics that appears as a self-organized chaotic system in which independent mechanisms co-work (Bak and Tang, 1989; Riguzzi et al., 2010).

Since the recognition of a mean westerly migration of plate boundaries and the net rotation of the lithosphere relative to the underlying mantle (Le Pichon, 1968; Knopoff and Leeds, 1972), several

papers suggested the tidal drag as a driving force of plate tectonics (Bostrom, 1971; Nelson and Temple, 1972; Moore, 1973). However, this model was abandoned because of the inferred high viscosity of the asthenosphere, where the decoupling is expected (Jordan, 1974), despite several articles claiming for much lower viscosity values in the low-velocity zone atop the asthenosphere (Jin et al., 1994; Pollitz et al., 1998; Mei et al., 2002).

However, the mainstream of plate motions along a flow exemplified by its tectonic equator (Crespi et al., 2007; Cuffaro and Doglioni, 2018), and the overwhelming evidence of polarized plate tectonics (Doglioni and Panza, 2015; Ficini et al., 2017, 2020) support an astronomical control of plate tectonics given by the combination of the Earth's rotation and the gravitational attraction of Moon and Sun. The asymmetries between subduction zones with opposed geographic polarity point for a tidal control on plate motions (Doglioni, 1994; Scoppola et al., 2006; Doglioni et al., 2007; Carcaterra and Doglioni, 2018). Asymmetries among the two sides of oceanic rifts that could be related to the net westerly directed rotation of the lithosphere are also evident

\* Corresponding author.

E-mail address: [carlo.doglioni@uniroma1.it](mailto:carlo.doglioni@uniroma1.it) (C. Doglioni).

**Table 1**

Tides with their periods and amplitudes are taken into account for the harmonic analysis of time series of the baselines of Figs. 1–9. In the first column the Doodson number; in the second the period and the amplitudes in the third. The values of the amplitudes and periods are in Cartwright and Edden (1973) and Kudryatsev (2004).

Low Frequency Solid Earth Tides		
Doodson Number	Period (days)	Amplitude (m)
0 5 8 5 5 4	121.752 (4 months)	0.00426
0 5 7 5 5 5	182.625 (6 months)	0.08565
0 5 6 5 5 4	365.264 (one year)	0.01360
0 5 5 7 6 5	1305.756 (3.57 years)	0.0009
0 5 5 6 5 5	3232.605 (8.85 years)	0.0003
0 5 5 5 7 5	3399.329 (9.3 years)	0.00064
0 5 5 5 6 5	6798.659 (18.61 years)	0.07119

(Doglioni et al., 2003; Panza et al., 2010; Chalot-Prat et al., 2017).

The pull of the Moon and Sun determines in the solid Earth the tidal bulge, which can be decomposed into its vertical and horizontal components that depend on latitude and may amount to 30–40 cm and 15–20 cm respectively for the M2, i.e., the semidiurnal tide, which has a period of about 12 h 25'. However, the tidal bulge is misplaced relative to the gravitational Earth-Moon alignment, being about 0.2°–0.3° (Munk, 1997; Gradstein et al., 2012) or up to 2.9° (Smith and Jungels, 1970; Lowrie, 2007) eastward of it, due to the delay in reaction for the anelastic component of the Earth (Agnew, 2007) as a response to the Moon's pull (Munk and McDonald, 1960). This misalignment determines the westerly-directed horizontal torque acting on the lithosphere (Scoppola et al., 2006) and the secular slowing of the Earth spin (Varga et al., 1998). Velocity gradients among plates can be interpreted

as controlled by viscosity changes in the planform of the decoupling layer atop the asthenosphere (Doglioni, 1993; Doglioni and Panza, 2015). The fastest plate is the Pacific moving WNW-ward relative to the mantle and having the lowest viscosity at its base (Pollitz et al., 1998). A contrast of 8–10 orders of magnitude in viscosity between the lithosphere and the underlying asthenosphere enhances relative decoupling in an oscillating system as body tides (Doglioni et al., 2011). As suggested by Varga and Grafarend (2018), to demonstrate a contribution of the body tides on plate motions and earthquakes, we need to consider their effects on the stress components acting parallel to the surface of the Earth. We provide here new data and new straightforward evidence for this model analysing the horizontal component of the body tide and comparing it with the speed of plates.

## 2. Data analysis of baselines among pairs of GNSS sites

In this work, an analysis of the relative motions of the main plates is carried out in search of the possible lunisolar tidal modulation. In particular, we examined both short and long-period analysis (Blewitt et al., 2018) of baselines bridging tectonic plates pairs and measured by geodetic techniques: Global Navigation Satellite System (GNSS), Satellite Laser Ranging (SLR) and Very Long Baseline Interferometry (VLBI) data are studied to check whether such lunisolar tidal modulation is present. Long-period harmonic analysis is made feasible since we have now geodetic stations all over the world for which data time series span up to 20–30 years. The velocity of the GNSS sites is routinely presented having removed the theoretical tide (Dach et al., 2015) which is a priori assumed having zero residual. Moreover, GNSS sites are affected by climatic seasonal atmospheric and tropospheric pressure oscillations and the variation of the pressure of the fluid in the underground due to climatic and phreatic cycles (Vespe et al., 2003; Tregoning and van Dam, 2005; Fu and Freymueller, 2012; Argus et al., 2014).

To overtake these limitations, the horizontal component of GNSS data has been analysed, in particular, the low frequency not affected by the aforementioned phenomena on sites with time series of about 7000–8000 days, e.g., about 19–21 years. Our analysis focuses on cross-

**Table 2**

Couples of GNSS stations used in the analysis.

Baselines involved in the analysis									
GPS station 1	Latitude	Longitude	Elevation (m)	Start of data acquisition	GPS station 2	Latitude	Longitude	Elevation (m)	Start of data acquisition
<b>Fig. 1 - LAMA</b> (Poland, Lamkowo)	53.892	20.670	187.010	1996	STJO (Canada, St. John's)	47.595	-52.678	152.833	1996
<b>Fig. 2 - ALIC</b> (Australia, Alice Springs)	-23.670	133.886	603.278	1996	LHAZ (China, Lhasa)	29.657	91.104	3624.577	1999
<b>Fig. 3 - MATE</b> (Italy, Matera)	40.649	16.704	535.663	1996	PIE1 (USA, Pie Town)	34.302	-108.119	2347.759	1996
<b>Fig. 4 - ARTU</b> (Russia, Arti)	56.430	58.560	247.588	1999	MDVJ (Russia, Mendeleevo)	56.021	37.215	257.150	2001
<b>Fig. 5 - DUBO</b> (Canada, Erickson Point)	50.259	-95.866	245.265	1996	WTZR (Germany, Wettzell)	49.144	12.879	666.034	1996
<b>Fig. 6 - HOFN</b> (Iceland, Hofn)	64.267	-15.198	82.712	1996	REYK (Iceland, Reykjavik)	64.139	-21.955	93.040	1996
<b>Fig. 7 - SANT</b> (Chile, Santiago)	-33.150	-70.669	723.064	1996	WGTN (New Zealand, Wellington)	-41.323	174.806	26.059	1996
<b>Fig. 8 - INVK</b> (Canada, Inuvik)	68.306	-133.527	46.451	2001	NRIL (Russia, Norilsk)	69.362	88.360	47.902	2000
<b>Fig. 9 - AIRA</b> (Japan, Aira)	31.824	130.600	314.650	1998	KOKB (Hawaii, Koke'e State Park)	22.126	-159.665	1167.348	1996
<b>Figs. 15-16 - MQZG</b> (New Zealand, McQueens Valley)	-43.703	172.655	154.681	1999	WGTN (New Zealand, Wellington Airport)	-41.323	174.806	26.059	1996

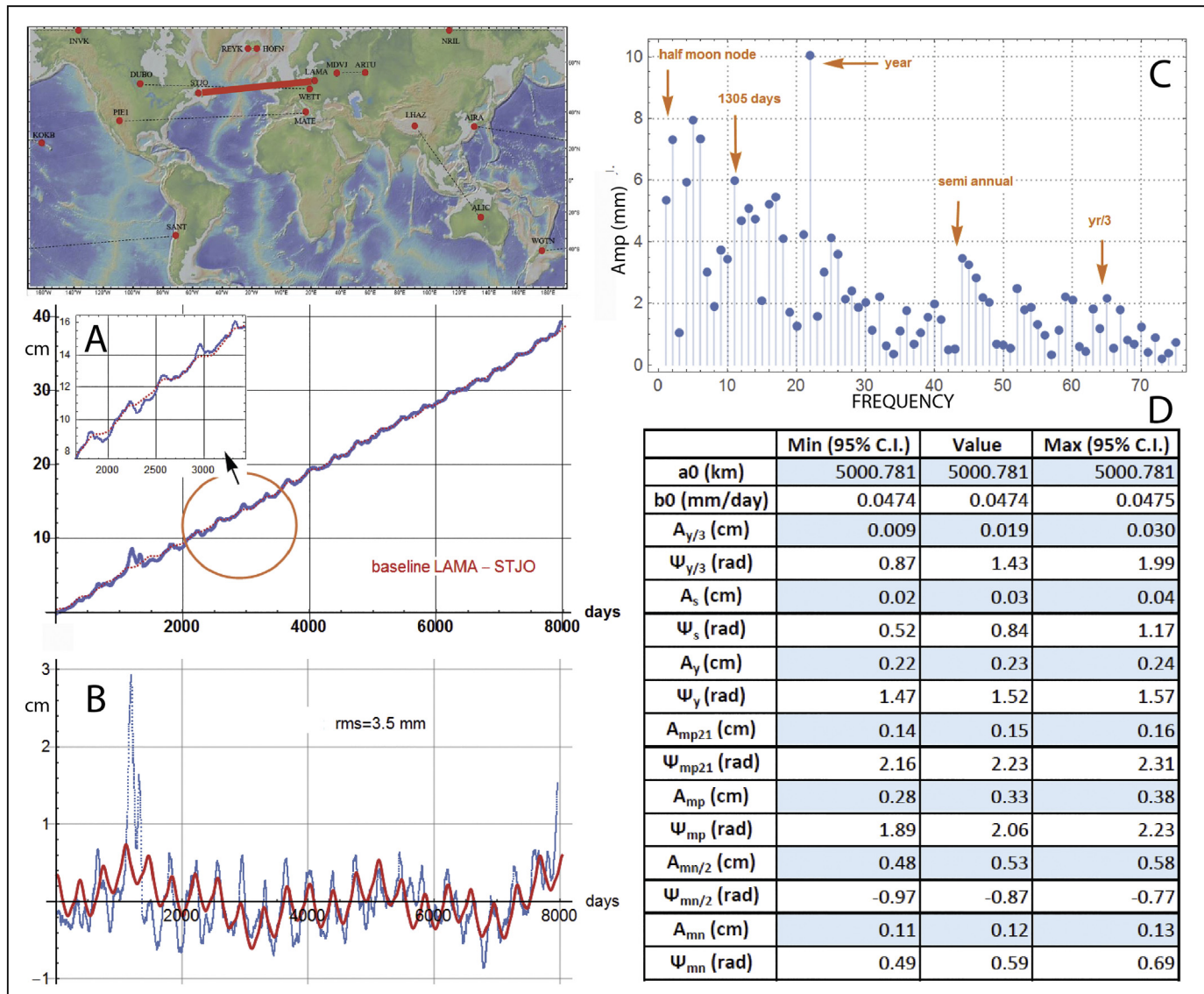


**Fig. 1.** Tidal modulation of plate velocity between North America and Europe. (A) GNSS data showing the lengthening between the LAMA site in Lamkowko (Poland) and STJO site in St. John's (Newfoundland) between 1997 and 2018. Notice the correlation between the data (blue dots), and the horizontal tidal component (red line). The spike on the left is due to antenna maintenance at the LAMA station. (B) Plot of the residuals; the plot was obtained by subtracting a slope equal to about 17.2 mm/yr. The blue dots are the values of the residuals after having applied a Moving Average over 30 days of data, whereas the red line is the function resulting from the non-linear least-square fitting of Eq. 3. The residuals of the fit are of only 3.5 mm even if it seems a jump occurred at the 4th year of acquisition. (C) The Fast Fourier Transform (FFT) analysis shows the presence of strong amplitudes of the tidal terms involved in the fitting. The frequency along the x-axis, is expressed in number of cycles over the time length of data. (D) Table of the data and tidal harmonics. The high quality of this time series is mainly because it is longer than the tidal term of 18.6 years and the data acquisition has been continuing and without external disturbances. For each tidal harmonics fitted yr/3, yr/2, yr, 1305 days, moon perigee, (moon node)/2 and moon node, we have listed the estimated amplitude and phase of each harmonic (third column); while the values of the second and fourth columns define the confidence interval (C.I.) at the level of 95%, confirming the tidal signatures. The first two rows define the parameters of the fitted slope ( $a$  and  $b$ ):  $y = a_0 + b_0 * t$ , where  $a_0$  is an initial length of the baseline and  $b_0$  is the velocity represented by the slope. The tidal frequency is known, and harmonics derive from Eq. 2.  $A$  is the amplitude and  $\Psi$  the phase respectively of each harmonic per 1/3 year (yr/3), semiannual (s), or annual (yr), twice the frequency of the Moon node and the frequency of the Moon perigee (mp21; i.e. 1305 days), the Moon perigee (mp), twice the frequency of the Moon node (mn/2), and the frequency of the Moon node (mn). (For interpretation of the references to colour in this figure legend, the reader is referred to the web version of this article.)

correlating different time-series of the lunisolar tidal modulation. A powerful way to assess whether tides have a significant effect on tectonic movements is to study the long periodic harmonics (LPH). LPH tides due to moon perigee and node precession on long time series of geodetic baselines provide a suitable strategy to single out such relationship. We use harmonic signals with periods longer than one month. In Table 1 are listed the main low-frequency tides and expected amplitudes and in Table 2 the data of the ten selected pairs of sites and related baselines. Nine baselines are presented in Figs. 1–9. The strategy consists in measuring the changes in the distance between many pairs of

GNSS stations located at different latitudes and longitudes and also in different geodynamic environments. If the tidal forces influence tectonics, the relative plate speed must contain a compatible modulation with changes in lunar distance and solar distance.

Furthermore, we performed a Fast Fourier Transform (FFT) analysis that shows the presence of semiannual, annual and signals compatible with the period of the lunar perigee harmonics. They exhibit non-negligible amplitudes that emerge with even greater clarity eliminating spurious very high-frequency contributions. Fig. 1 shows the analysis of GNSS data recording the lengthening of the baseline between the sites

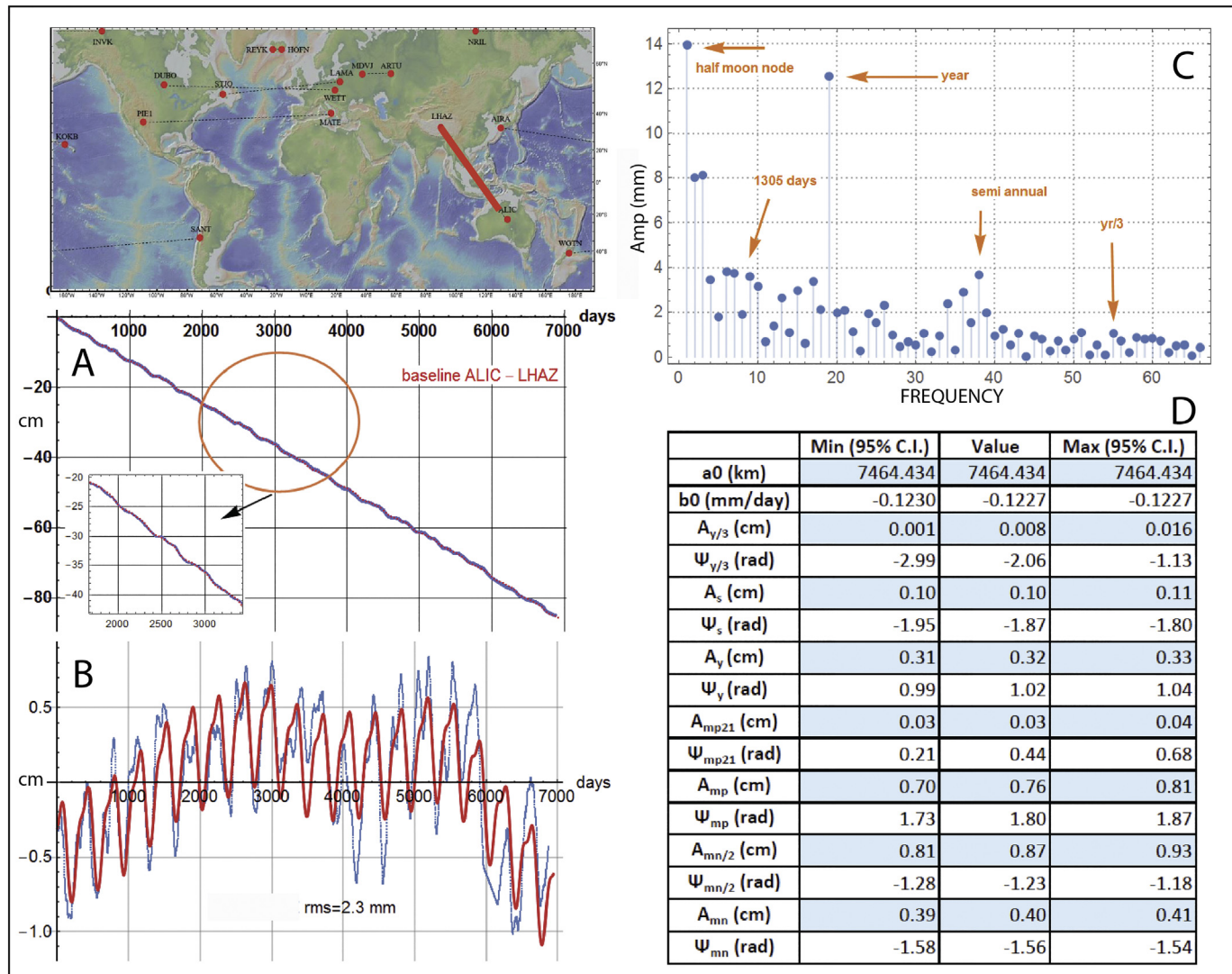


**Fig. 2.** Tidal modulation of plate velocity between Asia and Australia. (A) GNSS data showing the contraction between the ALIC stations in Central Australia (near the town of Alice Springs), and LHAZ (Lhasa) in Tibet (China) from 2000 until 2018. (B) Plot of the residuals of the distance between the two sites. The plot was obtained by subtracting a slope of about  $-44.8$  mm/yr. The blue dots represent the experimental data while the red curve corresponds to the expected theoretical trend. The residuals of the fit have a  $\sigma \approx 2.3$  mm. (C) The FFT analysis shows the meaningful presence of the harmonics selected to perform the non-linear. Also, in this case, there is a strong periodicity of 18.6 yr, with an amplitude of  $\approx 14$  mm. Experimental data show some gaps due to seismic events or to failure of geolocation devices. The frequency is expressed in number of cycles. (D) Table of the data and tidal harmonics. The high quality of this time series is mainly because it is longer than the tidal term of 18.6 years. The C.I. at the level of 95%, i.e.  $2\sigma$  level of the amplitudes estimated by the fit, confirm the tidal signatures. Legend as in Fig. 1. (For interpretation of the references to colour in this figure legend, the reader is referred to the web version of this article.)

LAMA in Poland (Eurasia plate) and STJO in Newfoundland (North America plate), mostly dictated by the Mid Atlantic Ridge spreading of about 2 cm/yr. The data (blue line of Fig. 1A) are filtered at low frequency and they are marked by oscillations of the horizontal extension rate. The tidal harmonics (red dashed line of Fig. 1A) almost overlap the data, indicating a correlation between sites speed and tidal modulation. The comparison of the theoretical and measured tidal component shows minimum residuals, supporting cause-effect among data and model. In the least-square fit, we used three-yearly harmonics (yr, yr/2 and yr/3) and four long periodic ones having Doodson numbers (0,5,5,6,5) of 18.6 yr, (0,5,5,7,5) of 9.3 yr, (0,5,5,6,5,5) of 8.85 yr and (0,5,5,7,6,5) of 1305 days. The signature of 8.85 should be small and undistinguishable with that due to half the moon nodal nutation/precession 9.3 yr long. For this reason, we have flagged on the FFT plot (Fig. 1, C) only the spikes as due to the harmonic 9.3 yr long. In FFT the spike due to the tide 18.6 yr long cannot be enhanced because it would require a time series at least twice longer than the investigated time

frame. Moreover, the FFT of residuals (Fig. 1C) and the root mean squares (Fig. 1D) highlight the following peaks at the Moon node, half Moon node, 1305 days, year, half-year and four yr/3. The statistical analysis is supported by the confidence intervals at the level of 95%, i.e. 2 levels of the amplitudes. The observation times necessary to appreciate the sought after-effects are quite long because of numerous sources of disturbance of the high-frequency signal, local phenomena and to the non-linear response of the lithosphere and the underlying mantle.

Besides the semidiurnal oscillation, there are six other fundamental harmonic frequencies (Munk and McDonald, 1960): the day (23 h 56' 4''), the Tropical month (27.322 days), the Solar year (365.256 days), the Lunar perigee (8.847 years), the Lunar nodes (18.613 years) and the precession of equinoxes (25,772 years).

In our analysis, we observed modulations in plate motion compatible with the Solar year, the period of the Lunar perigee and Lunar nodes. These results show clearly the influence of lunar and solar tidal

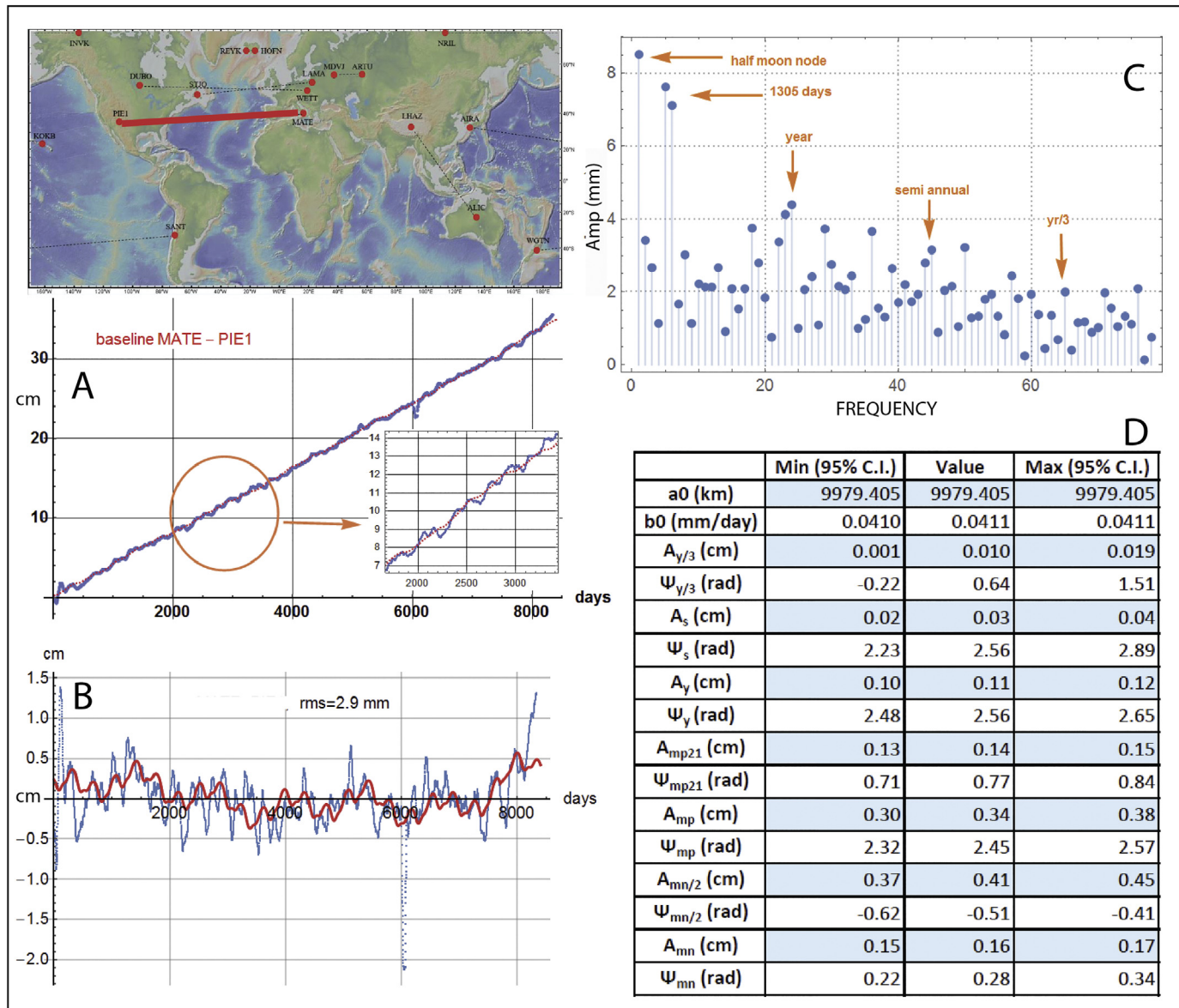


**Fig. 3.** Tidal modulation of plate velocity between southern Italy and the western United States. (A) GNSS data showing the contraction between Matera in southern Italy (MATE) and New Mexico (PIE1) stations from 1996 until 2018. (B) Plot of the residuals of the distance between the two sites. The plot was obtained by subtracting a slope of about 15 mm/yr. The blue points represent the experimental data while the red curve corresponds to the expected theoretical trend. The residuals of the fit have a  $\sigma \approx 2.9$  mm. (C) The FFT analysis shows the meaningful presence of the harmonics selected to perform the non-linear. Also, in this case, there is a strong periodicity of 18.6 yr, with an amplitude of  $\approx 8.5$  mm. Experimental data show some gaps due to seismic events or to failure of geolocation devices. The frequency is expressed in number of cycles. (D) Table of the data and tidal harmonics. The high quality of this time series is mainly because it is longer than the tidal term of 18.6 years and the data acquisition has been continuing and without external disturbances. It can be read as the same table in Fig. 1. (For interpretation of the references to colour in this figure legend, the reader is referred to the web version of this article.)

forces on the plate motion.

Although the most important tides features are diurnal and semi-diurnal (Cartwright and Edden, 1973; Kudryavtsev, 2004) they cannot play an active role in the modulation of plate motions due to the minimum value expected for the viscosity of the LVZ, which introduces a low pass filter that strongly attenuates the tidal signals with semi-daytime, diurnal and monthly frequencies (as shown in detail in the last paragraph of the article). The monthly, half-yearly and yearly features of the tides are mixed with other very strong geophysical and geodynamic effects: subsidence, water loading, earth's rotation, seasonal and climate weather changes, ocean circulation, etc., which make very difficult to extract the contribution of the tides and which sometimes contribute to reinforcing the astronomical signals that would otherwise be more attenuated. We define long periodic terms those harmonics

where both the daily and monthly contribution are zero, i.e. with the first two Doodson numbers 0 and 5 respectively. We have selected the most important long periodic tide harmonics according to the Kudryavtsev (2004) tables. The period of the tide is computed as follows:

$$T = [(\bar{\mathbf{D}} - \bar{\mathbf{O}}) \cdot \bar{\mathbf{f}}]^{-1} \quad (1)$$

Where  $\bar{\mathbf{D}}$  is the Doodson number,  $\bar{\mathbf{O}}$  is the Doodson zero vector (0,5,5,5,5,5) and  $\bar{\mathbf{f}}$  is the vector of the tidal fundamental frequencies expressed in terms of 1/day: (1/0.9972, 1/27.3, 1/365.25, 1/(8.85 × 365.25), 1/(18.6 × 365.25) and 1/(25,772 × 365.25).

We deem long periodic terms those harmonics longer than a year. Table 1 shows the most important tidal harmonics involved in the non-linear fit of Eq. 2. In the first column the Doodson numbers are given, in

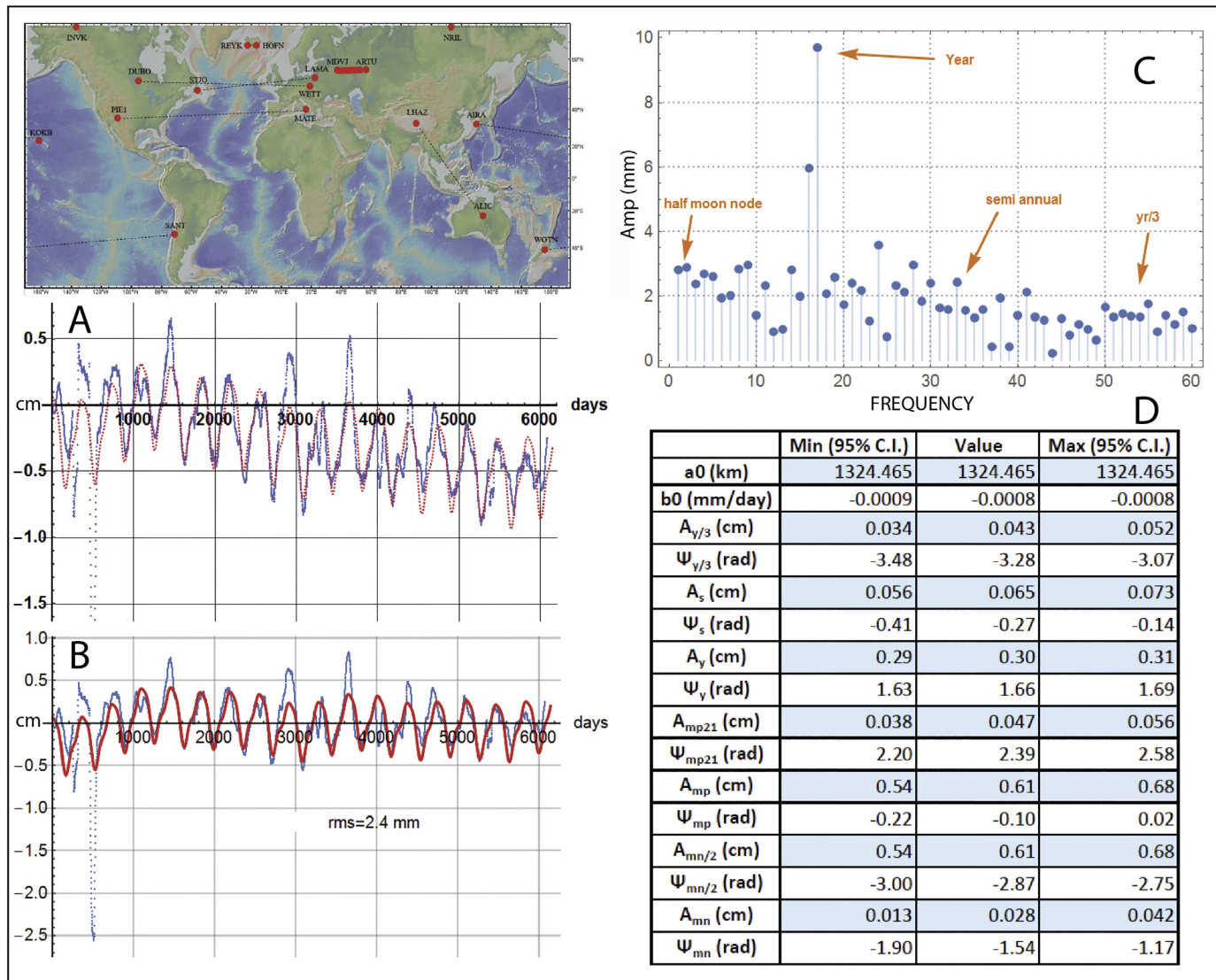


**Fig. 4.** Tidal modulation of plate velocity between two sites in Russia. (A) GNSS data showing the small contraction between the ARTU and MDVJ stations in Siberia from 2002 until 2018. (B) Plot of the residuals of the distance between the two sites. The plot was obtained by subtracting a slope of about  $-0.2 \text{ mm/yr}$ . The blue points represent the experimental data while the red curve corresponds to the expected theoretical trend. The residuals of the fit have a  $\sigma \approx 2.4 \text{ mm}$ . (C) The FFT analysis shows the meaningful presence of the harmonics selected to perform the non-linear. In this case, the harmonic of 18.6 yr is an order of magnitude smaller with respect to baselines at the same latitude and with a similar length ( $0.28 \pm 0.07 \text{ mm}$ ). On the contrary, the annual term is strong. Experimental data show some gaps due to seismic events or to failure of geolocation devices. The frequency is expressed in number of cycles. (D) Table of the data and tidal harmonics. The high quality of this time series is mainly because it is longer than the tidal term of 18.6 years. The C.I. at the level of 95%, i.e.  $2\sigma$  level of the amplitudes estimated by the fit, confirm the tidal signatures. Legend as in Fig. 1. (For interpretation of the references to colour in this figure legend, the reader is referred to the web version of this article.)

the second the period of the harmonics (days) and in the third the amplitude of the tide (in meters). We have added in the harmonic analysis high frequency features too (yearly, semiannual and 1/3 of the year) which are mainly ruled by the exchange of angular momentum between the gaseous and fluid layers and the solid earth, atmospheric and ocean loading, Earth's rotation parameters etc. (Vespe et al., 2003; Altamimi et al., 2016). We have added these features in spectral analysis, despite the small tidal contribution, because otherwise the evidence of long periodic moon tides signatures could be erroneously estimated. The goal of our work is indeed to demonstrate that there are elastic horizontal vibrations of long baselines induced by the moon tides which modulate secular drift of the tectonic plates.

We base our analysis on data sets acquired from stations with at least 17–22 years-long activity. The GNSS stations allow us to observe with great precision (horizontal ground movements over a long period). To understand whether tidal modulations are present in plate motion,

we looked for the main tidal harmonic signals in the movements of the baselines just described. We selected ten pairs of sites that are listed in Table 2.

The baseline in Fig. 2 shows the trend of the distance between the ALIC station, located near Alice Springs in the Northern Territory in Australia, and LHAZ in Tibet: these stations were chosen because of their location so far from the oceans so that the ocean-loading effect is minimized allowing in this way to exclusively highlight the contributions of the solid tide eliminating possible effects due to liquid tide. The baselines of Figs. 1, 3, 5 and 6 contain the movements between the North American plate and the Eurasian plate at different latitudes respectively between LAMA in Poland and STJO in Newfoundland, MATE near Matera in Italy and PIE1 in Pie Town, New Mexico, USA; DUBO station, not far from Winnipeg in Manitoba, and WTZR at Wettzell in Germany and HOFN near the homonymous town in Iceland and REYK in the west of the country.

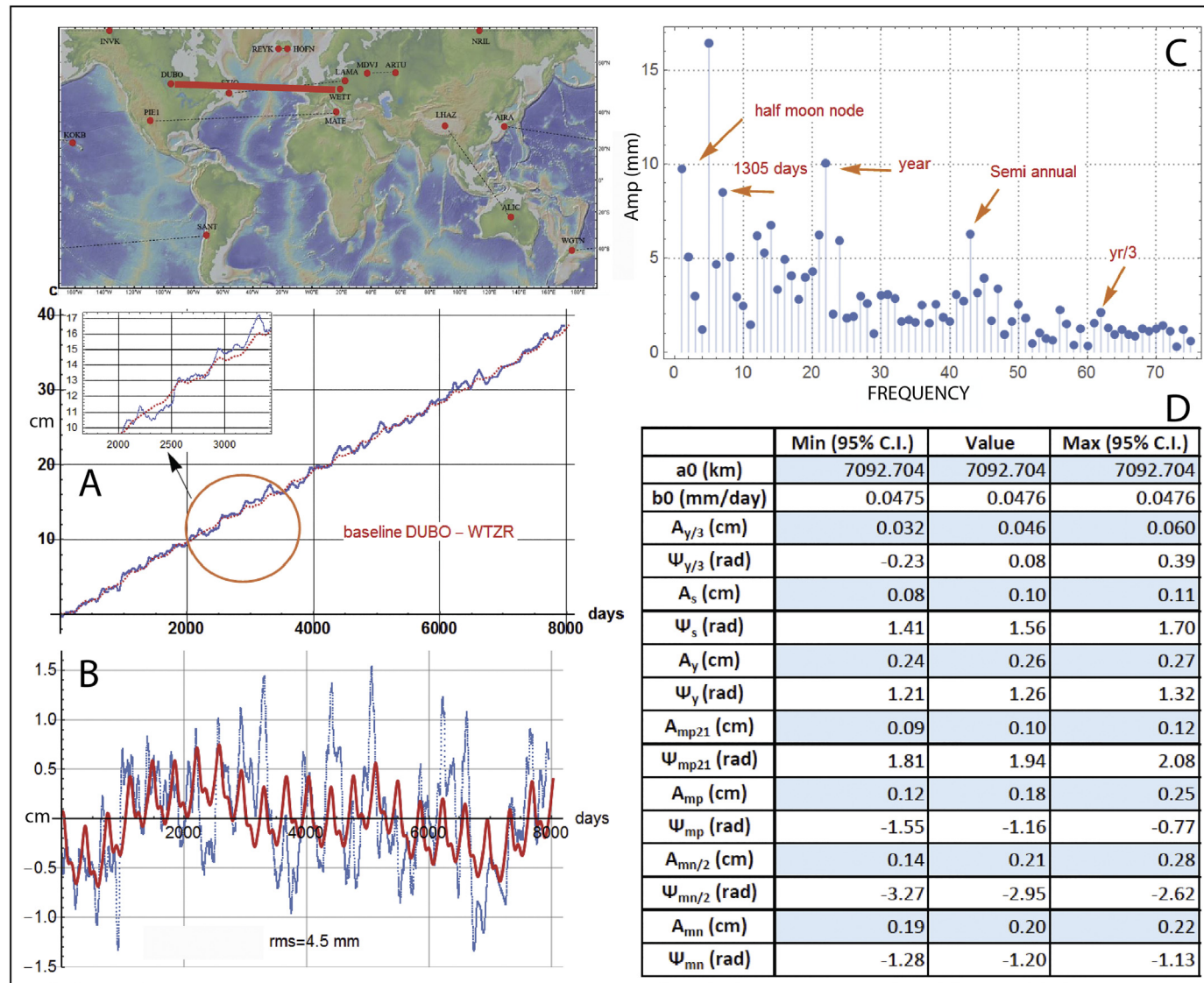


**Fig. 5.** Tidal modulation of plate velocity between central Canada and Germany. (A) GNSS data showing the extension between the DUBO in Canada and Wettzell in Germany (WTZR) stations from 1997 until 2018. (B) Plot of the residuals of the distance between the two sites. The plot was obtained by subtracting a slope of about 17.4 mm/yr. The blue points represent the experimental data while the red curve corresponds to the expected theoretical trend. The residuals of the fit have a  $\sigma \approx 4.5$  mm. (C) The FFT analysis shows the meaningful presence of the harmonics selected to perform the non-linear fit. Also, in this case, there is a strong periodicity of 18.6 yr, with an amplitude of  $\approx 10$  mm. Experimental data show some gaps due to seismic events or to failure of geolocation devices. The frequency is expressed in number of cycles. (D) Table of the data and tidal harmonics. The high quality of this time series is mainly because it is longer than the tidal term of 18.6 years. The C.I. at the level of 95%, i.e.  $2\sigma$  level of the amplitudes estimated by the fit, confirm the tidal signatures. Legend as in Fig. 1. (For interpretation of the references to colour in this figure legend, the reader is referred to the web version of this article.)

The baseline of Fig. 4 ARTU and MDVJ stations in Siberia is the unique place within the same plate. This is particularly important in our analysis because we expect that the moon tides exert lower stress on such baselines.

SANT (Santiago de Chile) and WGTN (Wellington, New Zealand) stations (Fig. 7) have allowed us to monitor the cumulate movements between the South American plate, Nazca plate, and the margin between the Australian and Pacific plate, crossing both western and eastern Pacific subduction zones, and the East Pacific Rise over a twenty years-long period. The analysed baselines are listed in Table 2.

The baseline of Fig. 8 refers to the movement observed between the INV station in the Northwestern Territories in Canada and NRIL in the Territory of Krasnoyarsk in central Siberia, it allows us to observe tidal modulations in the motion between the North American plate and the Eurasian plate in the high latitude (N). The baseline pair formed by AIRA station, near the city of Aira in Kagoshima Prefecture in Japan

and KOKB in the Hawaii Islands (Fig. 9) allows us to observe the relative displacements between the Eurasian Plate and the Pacific Plate over about twenty years. LPH tides due to moon perigee and node precession imprinted on long time series of geodetic baselines are the possible strategy to adopt to single out such relationship.

Once we have selected the baselines, we have applied the following steps:

- 1) A moving average (MA) over 30 days is performed to smooth the data time series. In such a way the flickering up to monthly frequency is damped to lower the level of random errors.
- 2) After MA, the FFT is applied to identify other meaningful features. In all the analysed data series yearly, semiannual and one-third of the year features emerge. Furthermore, the feature twice the frequency of nodal moon which almost overlap the frequency of moon perigee precession is very strong as well. Surprisingly the feature

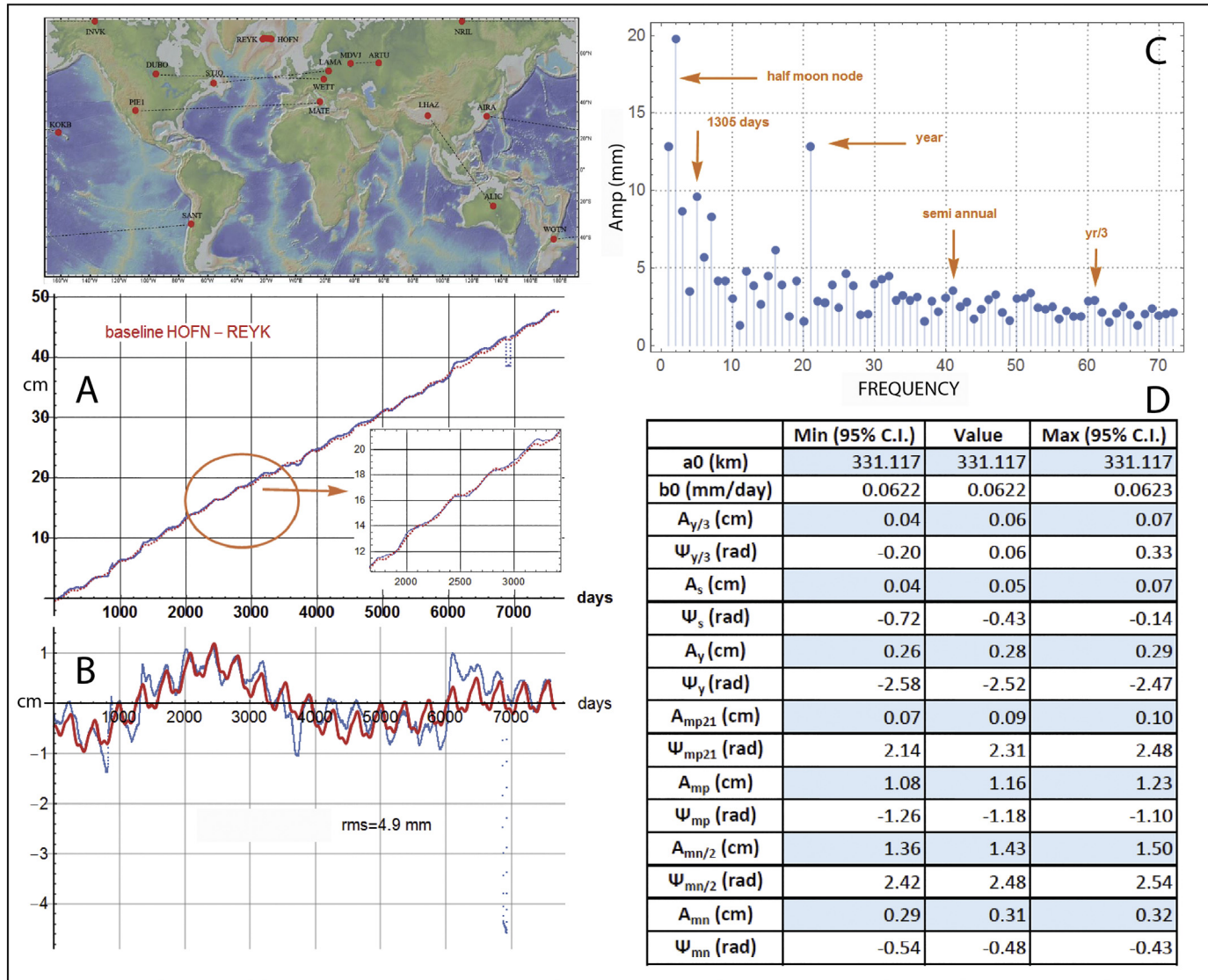


**Fig. 6.** Tidal modulation of plate velocity between two sites in Island across the Mid Atlantic Ridge. (A) GNSS data showing the extension between the HOFN and REYK stations from 1998 until 2018. (B) Plot of the residuals of the distance between the two sites. The plot was obtained by subtracting a slope of about 22.7 mm/yr. The blue points represent the experimental data while the red curve corresponds to the expected theoretical trend. The residuals of the fit have a  $\sigma \approx 4.9$  mm. (C) The FFT analysis shows the meaningful presence of the harmonics selected to perform the non-linear. Also, in this case, there is a strong periodicity of 18.6 yr, with an amplitude of  $\approx 13$  mm. Experimental data show some gaps due to seismic events or to failure of geolocation devices. The frequency is expressed in number of cycles. (D) Table of the data and tidal harmonics. The high quality of this time series is mainly because it is longer than the tidal term of 18.6 years. The C.I. at the level of 95%, i.e.  $2\sigma$  level of the amplitudes estimated by the fit, confirm the tidal signatures. Legend as in Fig. 1. (For interpretation of the references to colour in this figure legend, the reader is referred to the web version of this article.)

given by the combination of two times the frequency of moon node and the moon perigee (055675 as Doodson number), with a corresponding period of 1305 days, emerges meaningfully.

3) Thus, together with the period of moon perigee and node, we add five more features of the period: 121.75, 182.625, 365.264, 1305.764 and 3292.660 days. It is well known that FFT is a bad estimator of the amplitude. Furthermore, it detects harmonics with a period of up to half of the length of the time series. The moon node period is instead almost long as GNSS data time series. For these reasons, to estimate the amplitudes and phases of the selected harmonics included the moon nodal term, a non-linear least-square fit of data has been performed (Vespe et al., 2002), applied to the following relationship:

$$y(t) = a + b \cdot t + \sum_i^n A_i \sin(2 \cdot \pi \cdot \beta_i \cdot t + \varphi_i) \quad (2)$$

Where  $y(t)$  are the observations  $a$  and  $b$  are the slope and the initial length of the baseline,  $\beta_i$  represents the  $i^{\text{th}}$  Doodson frequency,  $\varphi_i$ ,  $A_i$  are, in turn, the phase and the amplitude of the trigonometric functions, which represent the harmonics involved in the Eq. 2.  $a$ ,  $b$ ,  $\varphi_i$ ,  $A_i$  are the parameters to be estimated; while  $t$  is the unique variable of the model. The linear coefficients  $a$  and  $b$  are estimated first applying a classical linear least-squares fit of baselines data:  $y_k$ . In a second step, the trigonometric parameters are estimated applying a non-linear Levenberg–Marquardt fit (Bates and Watts, 1988, and implemented in calculus software “Mathematica”) to minimize the following residual function:

$$\sum_k \left\| R(t_k) - \sum_i^n A_i \sin(2 \cdot \pi \cdot \beta_i \cdot t_k + \varphi_i) \right\|^2 \quad (3)$$

$$R(t_k) = y_k - (a_0 \cdot t_k + b_0)$$

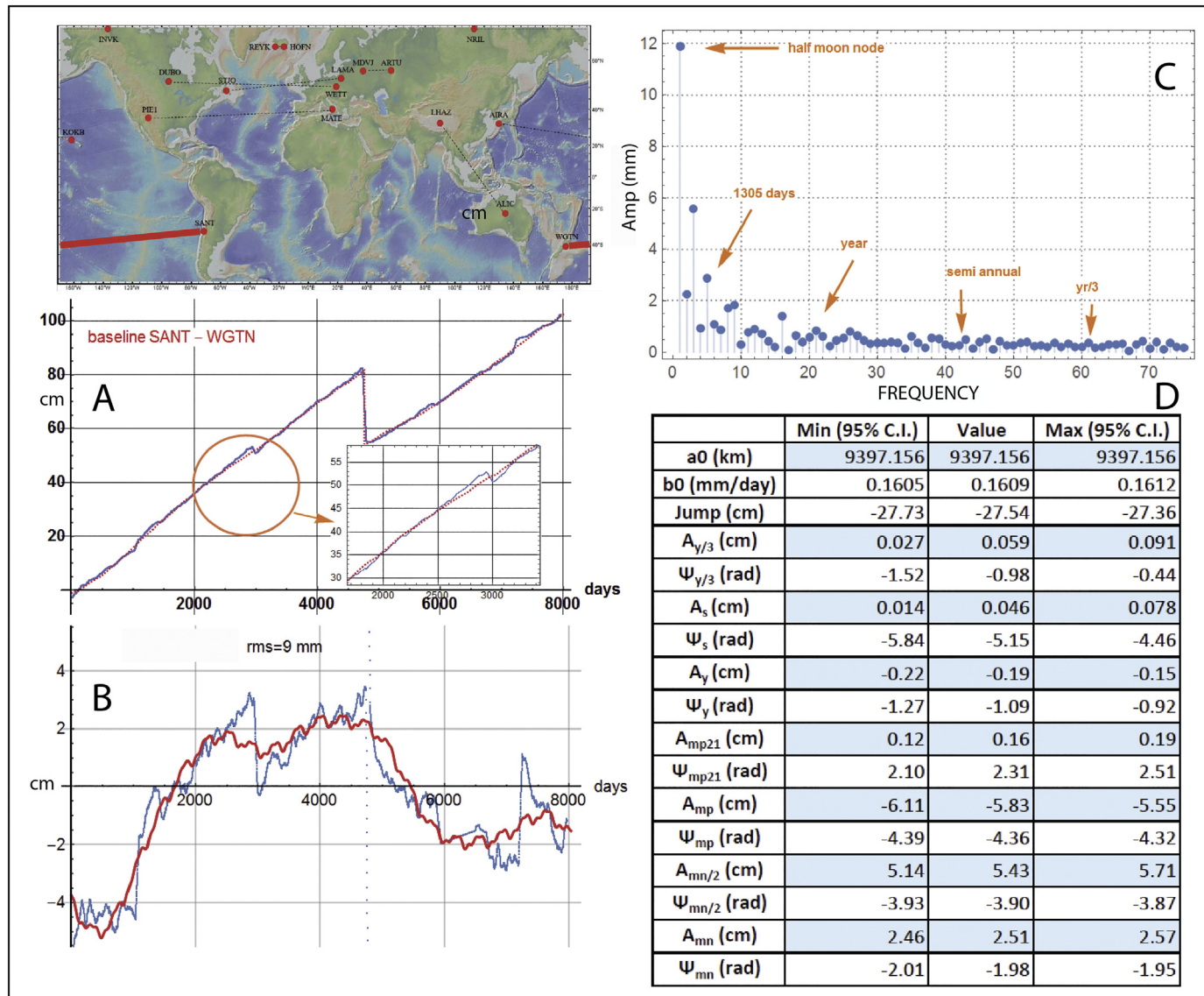


**Fig. 7.** Tidal modulation of plate velocity between New Zealand and Chile. (A) GNSS data showing the contraction between Wellington (WGTN) and Santiago (SANT) stations in New Zealand, and Chile, from 1997 until 2018. (B) Plot of the residuals of the distance between the two sites. The plot was obtained by subtracting a slope of about  $-58.7$  mm/yr. The blue points represent the experimental data while the red curve corresponds to the expected theoretical trend. The residuals of the fit have a  $\sigma \approx 9$  mm. (C) The FFT analysis shows the meaningful presence of the harmonics selected to perform the non-linear fit. The strongest periodicity of the half Moon node has an amplitude of  $\approx 12$  mm. Experimental data show some gaps due to seismic events or to failure of geolocation devices, e.g., the February 27th, 2010, Mw 8.8 Maule earthquake that generated a jump backwards of more than 27 cm. The frequency is expressed in number of cycles. (D) Table of the data and tidal harmonics. The high quality of this time series is mainly because it is longer than the tidal term of 18.6 years. Anyway, for this baseline, we have listed also the estimated jump due to Maule earthquake. The C.I. at the level of 95%, i.e.  $2\sigma$  level of the amplitudes estimated by the fit, confirm the tidal signatures. Legend as in Fig. 1. (For interpretation of the references to colour in this figure legend, the reader is referred to the web version of this article.)

where  $R(t_k)$  are the residuals coming from the linear least-square fit,  $y_k$  are the observations and  $a_0$  and  $b_0$  are the estimated coefficients of the linear slope. In Figs. 1–9  $a_0$  and  $b_0$  are reported in the results of the plots. The behaviour of the computed slope + harmonics (red line), compared against the real measurements of baselines performed on weakly rate (blue dots), is shown in Figs. 1–9A. Figs. 1–9B show the comparison between the residuals  $R(t_k)$  coming from the preliminary linear fit (blue dots) and their non-linear fit with the 7 tidal harmonics selected as in Eq. 3. Figs. 1–9C show the FFT of the residuals  $R(t_k)$  where are underlined the features we have selected for the fitting. Figs. 1–9D report the tables where the results of the fit are summarized. In the table, we have included also the Confidence Intervals (C.I.) at the level of 95% ( $2\sigma$ ) of each parameter: offset, linear drift, amplitudes and phases of the harmonic terms.

Then for each solution, we have built the quadratic mean of the amplitudes for each baseline:

$$Amp = \sqrt{\sum_i^7 A_i^2} \quad (4)$$

Fig. 10 is a plot in which the relationship between  $Amp$  (y-axis) and the average latitude of the baselines (x-axis) is shown. The plot shows a good correlation between  $Amp$  and the latitude at the level of  $R \approx 0.85$ . The  $Amp$  decreases indeed with latitude relative to the tectonic equator, supporting its astronomical origin (Fig. 10). Finally, it is worthwhile to point out that Fig. 4 reports the results of the only intraplate baseline selected. In the results, there is an anomaly because the amplitude of the moon node harmonic is negligible, unlike what happens for the other baselines. This is crucial evidence that Moon tides trigger the

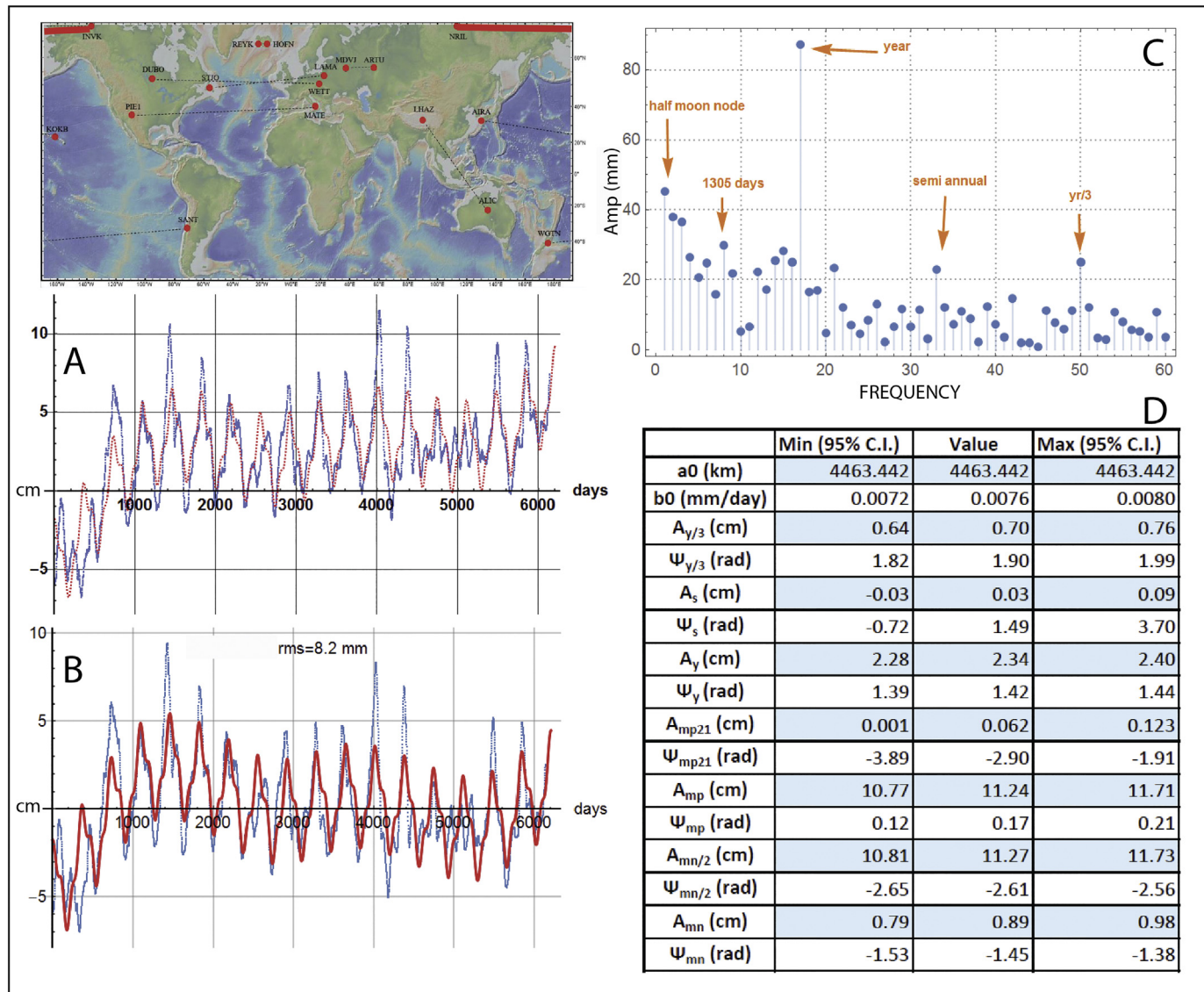


**Fig. 8.** Tidal modulation of plate velocity between Russia and Canada. (A) GNSS data showing the extension between the INVK and NRIL stations from 2002 until 2018. (B) Plot of the residuals of the distance between the two sites. The plot was obtained by subtracting a slope of about 2.8 mm/yr. The blue points represent the experimental data while the red curve corresponds to the expected theoretical trend. The residuals of the fit have a  $\sigma \approx 8.2$  mm. (C) The FFT analysis shows the meaningful presence of the harmonics selected to perform the non-linear. Also, in this case, there is a strong periodicity of 18.6 yr with an amplitude of  $\approx 6$  mm. Experimental data show some gaps due to seismic events or to failure of geolocation devices. The frequency is expressed in number of cycles. (D) Table of the data and tidal harmonics. The high quality of this time series is mainly because it is longer than the tidal term of 18.6 years. The C.I. at the level of 95%, i.e.  $2\sigma$  level of the amplitudes estimated by the fit, confirm the tidal signatures. Legend as in Fig. 1. (For interpretation of the references to colour in this figure legend, the reader is referred to the web version of this article.)

movements of the tectonic plates.

### 3. Single GNSS station versus tidal harmonics

We made a further test analysing the raw data of a single station, taking KOK5 (Hawaii chain) as an example, searching the lunisolar tidal harmonics present in the No-Net-Rotation Reference Frame (NNR, Argus and Gordon, 1991) motion and studying its amplitude and phase with respect to the horizontal tidal stress produced by the Moon and the Sun. In this way, it is possible to verify the presence of a phase shift between the NNR and the solid Earth tides or to hypothesize its substantial absence, at least at low frequency. The lunar and solar tides influence plate tectonics by inducing relative movements between the decoupled portions at the lithosphere base, i.e., in the low-velocity zone (LVZ). However, the role of the NNR model is not clear: is there a phase difference between the tidal stress and the speed that GNSS stations

show in NNR? The harmonics have different intensity ratios compared to the theoretical models: what can we infer about the physical properties of the LVZ?

We analysed the motion of the GNSS station, KOK5, Hawaii, USA, between 1997 and 2018, searching for the lunisolar tidal harmonics present in its NNR motion, in this way it is possible to verify the presence of a phase shift between NNR and the solid Earth tides or to hypothesize its substantial absence, at least at low frequency. The harmonics have different intensity ratios compared to the theoretical models. The main tidal harmonics are reported in Table 1. In this work, particular attention is paid to those with lower frequencies.

The processed GNSS data have been filtered by anthropogenic or anomalous signals, then a linear fit is subtracted to show the residuals. With a moving average filter of the signals with a period of fewer than 60 days, we obtain the residual displacements shown in Fig. 11. The high sampling of the Fast Fourier Transform (FFT) to achieve a good

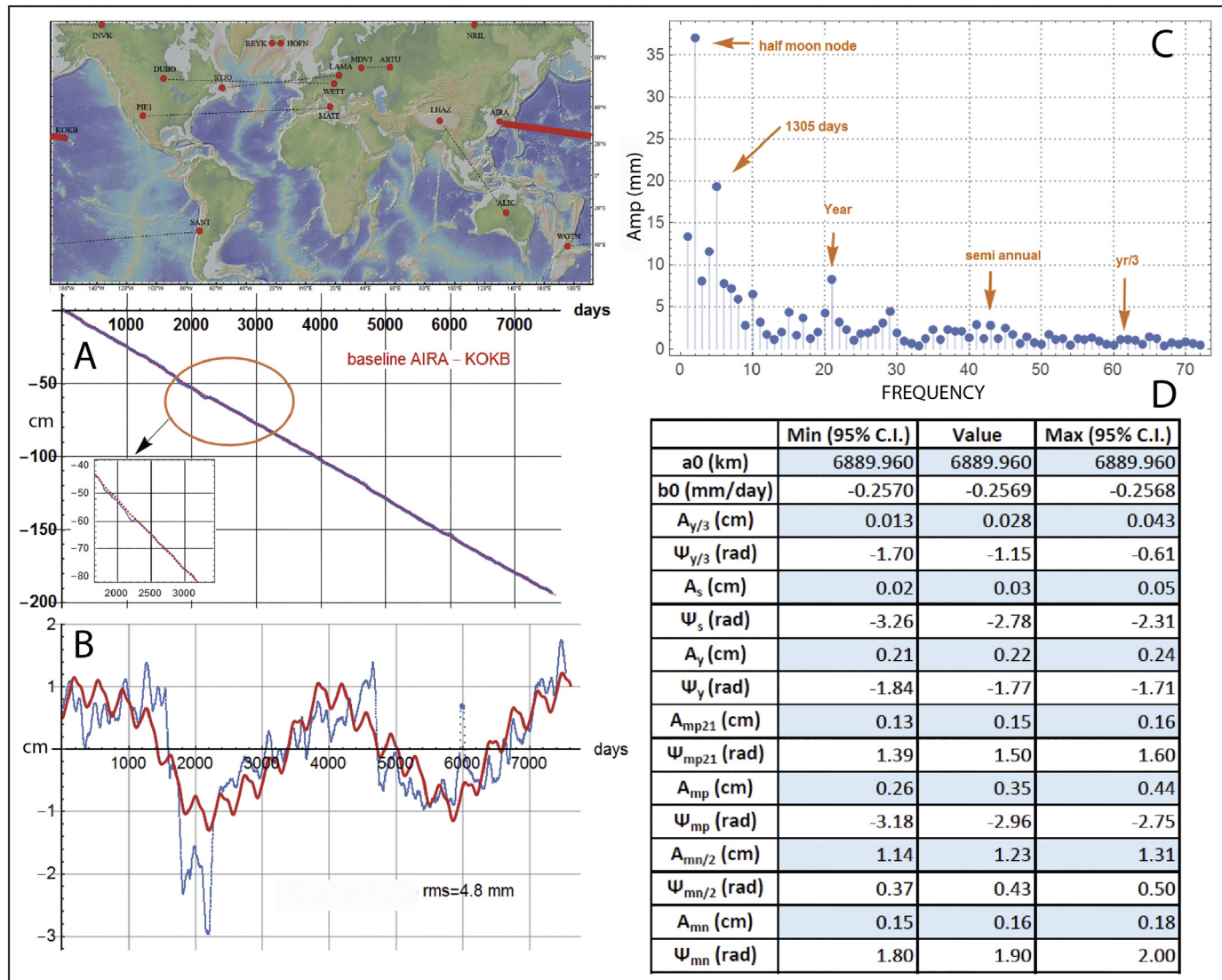


**Fig. 9.** Tidal modulation of plate velocity between Japan and Hawaii in the Pacific plate. (A) GNSS data showing the contraction between the AIRA and KOKB stations from 1998 until 2018. (B) Plot of the residuals of the distance between the two sites. The plot was obtained by subtracting a slope of about  $-93.8 \text{ mm/yr}$ . The blue points represent the experimental data while the red curve corresponds to the expected theoretical trend. The residuals of the fit have a  $\sigma \approx 4.8 \text{ mm}$ . (C) The FFT analysis shows the meaningful presence of the harmonics selected to perform the non-linear. In this case, there is a strong periodicity of the half Moon node, with an amplitude of  $\approx 37 \text{ mm}$ . Experimental data show some gaps due to seismic events or to failure of geolocation devices. The frequency is expressed in number of cycles. (D) Table of the data and tidal harmonics. The high quality of this time series is mainly because it is longer than the tidal term of 18.6 years. The C.I. at the level of 95%, i.e.  $2\sigma$  level of the amplitudes estimated by the fit, confirm the tidal signatures. Legend as in Fig. 1. (For interpretation of the references to colour in this figure legend, the reader is referred to the web version of this article.)

estimate of the harmonics in the residuals, identifies in particular two signals, one with a spectral intensity greater than 8 with period 18.60 years and amplitude of about 3 mm (Fig. 12) with its maximum at the beginning of 2008 (in-phase and with an intensity compatible with the harmonic relative to the lunar nodal precession) and an annual signal in phase with the lunisolar stress, with amplitude  $\sim 1/12$  of the harmonic with period 18.61 years (while theory predicts that it is  $\sim 1/5.23$  (Wahr, 1995). The horizontal component of the lunisolar tidal stress can be computed using the Love's theory (MacDonald, 1964) and the torque amount to  $4.8 \cdot 10^{16} \text{ Nm}$  (Shen and Nab, 2017) (Fig. 13).

This may mean that the top asthenosphere has an attenuation of the harmonic signals by a factor of  $\sim 2.29$  going from a period of 18.6 years to one of 1.0 years. This means that the Maxwell time of the decoupling layer at the lithosphere base in the low-velocity zone (LVZ) could be of the order of  $10^9 \text{ s}$ . If we compare this value with that of the crust or the upper mantle and considering the hypothesis of  $\eta \sim 10^{17} \text{ Pa s}$  (Hu et al., 2016) for the average viscosity of the asthenosphere at 200–300 Km

depth with a Maxwell time of the lithosphere of about  $10^{12} \text{ s}$ , for the LVZ we obtain a rough viscosity estimate of  $\eta \sim 10^{14} \text{ Pa s}$ . Moreover, the residuals do not distribute normally but follow the Generalized Extreme Value distribution. The residuals also show the presence of large deviations that scale with a power law. The displacement GPS data of the KOK5 station present harmonics compatible with the amplitude and phase of the lunisolar tidal stress. The NNR reference system does not show an appreciable phase shift concerning the lunisolar tidal stress.

Although the average viscosity value of the upper mantle is assumed  $10^{18}\text{--}10^{21} \text{ Pa s}$  (e.g., Cathles, 1975; Sabadini et al., 1991), mineral phases and chemical heterogeneities determine a stratification in the viscosity of the upper mantle, being the low-velocity zone the layer where the lowest values can be inferred. However, usual techniques in computing viscosity as glacial isostatic rebound assume vertical loading and unloading, whereas the viscosity calculated shearing the mantle can be lower of several orders of magnitude (Scoppola et al., 2006). The

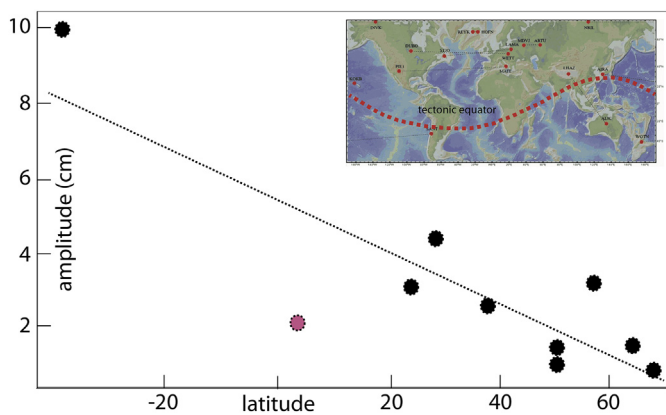


**Fig. 10.** Norm of the amplitudes (see tables D of Figs. 1, 2, S1-S7) versus latitude. It decreases toward the high latitude, but the peak is 28–30° misplaced in the southern hemisphere relative to the geographic equator. The correlation coefficient between the amplitudes and latitudes is  $R = 0.85$ . Notice that the tectonic equator has an angle of about 28–30° with respect to the equator (Crespi et al., 2007), being the projection of the average Moon orbit on the surface of the Earth. This would explain the larger residual in the southern hemisphere. The red dot corresponds to Fig. 2, which is crossing most of the southern hemisphere and is highly oblique to the tectonic equator, explaining the relatively low residual. (For interpretation of the references to colour in this figure legend, the reader is referred to the web version of this article.)

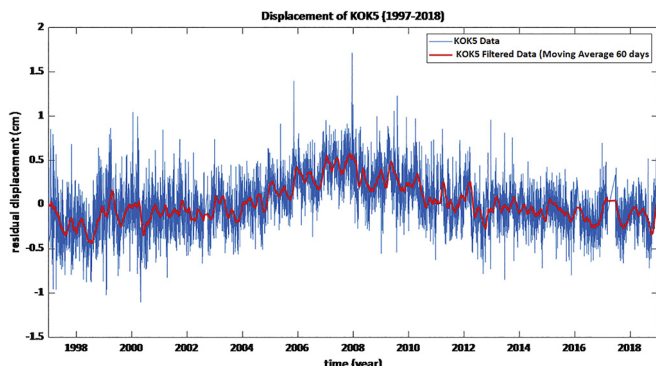


**Fig. 11.** Processed KOK5 (blue) data with replotted the filtered (Mov. Average 60 days) data (red line). (For interpretation of the references to colour in this figure legend, the reader is referred to the web version of this article.)

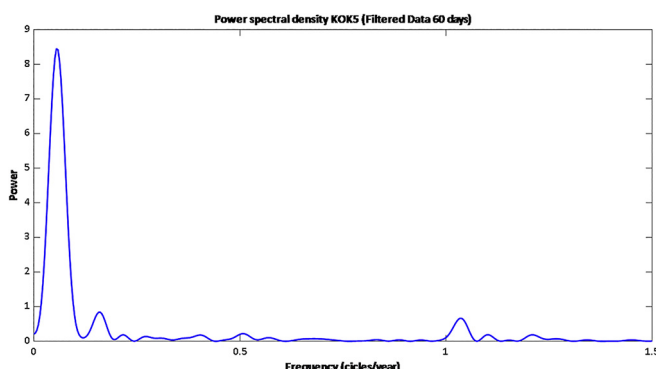


**Fig. 12.** Fast Fourier Transform density spectrum of the filtered KOK5 data by using a moving average filter (60 days). We have a strong peak at 0.05379 cycles/year, on the right a second signal corresponding to 6.21 years long period (1/3 of the lunar mode), and the Solar Annual Harmonic.

presence of the asthenosphere and a thin layer at its top, i.e., the low-velocity zone (between 100 and 200 Km depth, Fig. 17), makes it possible to decouple the lithosphere and the mantle under the action of

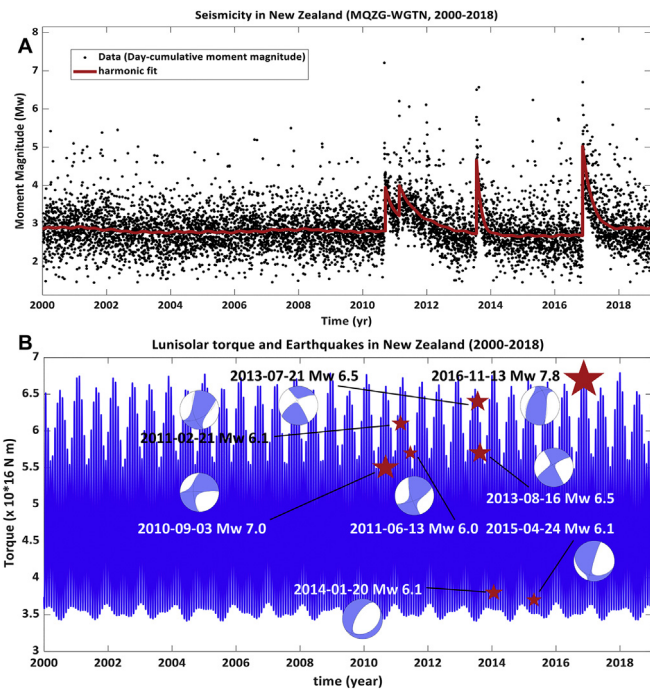


**Fig. 13.** The horizontal component of the lunisolar tidal stress modulates seismic activity in New Zealand. (A) Day-cumulated seismic energy, expressed in Mw, in New Zealand (considering seismic events with  $ML > 2.0$  occurred at a latitude between  $40.98^\circ$  S and  $44.25^\circ$  S and longitude between  $171.34^\circ$  E and  $175.47^\circ$  E, GeoNet Earthquake Catalogue for New Zealand, 2020) shows tidal modulations with not negligible amplitudes. The fit is performed using a function, which contains the tidal harmonics with 18.61, 9.3, 8.85, 4.4, 3.57, 1.0- and 0.5-year-long period and decreasing exponentials added in correspondence with the most significant seismic events. In particular, the most relevant oscillations are the 18.61 years-long periods harmonic with an amplitude, in terms of moment magnitude, of  $0.049 \pm 0.011$ , then 9.3 years with  $0.064 \pm 0.010$ , the harmonic with 4.4 years-long period  $0.031 \pm 0.007$ . (B) Tidal horizontal stress (calculated from lunar and solar ephemerides available at Nasa, 2020) and distribution of main seismic events ( $Mw > 6.0$ ) of the last twenty years in New Zealand represented with red stars, whose size is proportional to their moment magnitude. Strong earthquakes do not distribute uniformly over time, and extensional faults seismic events are favoured by low tidal stress values, while reverse/transpressional fault earthquakes are activated more easily during higher tidal stress. In particular, the Great Kaikoura Earthquake (14/11/2016,  $Mw 7.8$ ) occurred on the day of maximum stress over several years. Focal mechanisms from the USGS catalogue (United States Geological Survey, 2020). (For interpretation of the references to colour in this figure legend, the reader is referred to the web version of this article.)

low frequency lunisolar tidal forces. In fact, in the presence of a viscosity value equal to  $10^{13}$ – $10^{15}$  Pa s (Carcaterra and Doglioni, 2018), the Maxwell time is reduced from  $10^3$  years for the mantle to about  $10^9$  s (some decades) for the LVZ, therefore compatible with harmonics with more than one-year-long period identified in the Fourier analysis performed for all the aforementioned baselines. Significantly, the amplitudes of the of 18.6, 9.3 and 6.2 years-long period harmonics are substantially well proportioned in their amplitude, moreover, the annual solar tide is attenuated, although certainly amplified by seasonal and climate weather changes, while the six-month or higher frequency harmonics are very weak. This result does not change either by minimizing noise or carefully choosing the baseline to optimize the observation capacity of the higher frequency harmonics. Therefore, the low-velocity zone behaves like a low-pass filter attenuating the high-frequency harmonics as the viscosity value is too high, therefore in correspondence with these the LVZ has an almost fully elastic behaviour; decreasing the frequency, the elastic response disappears while the visco-plastic response increases.

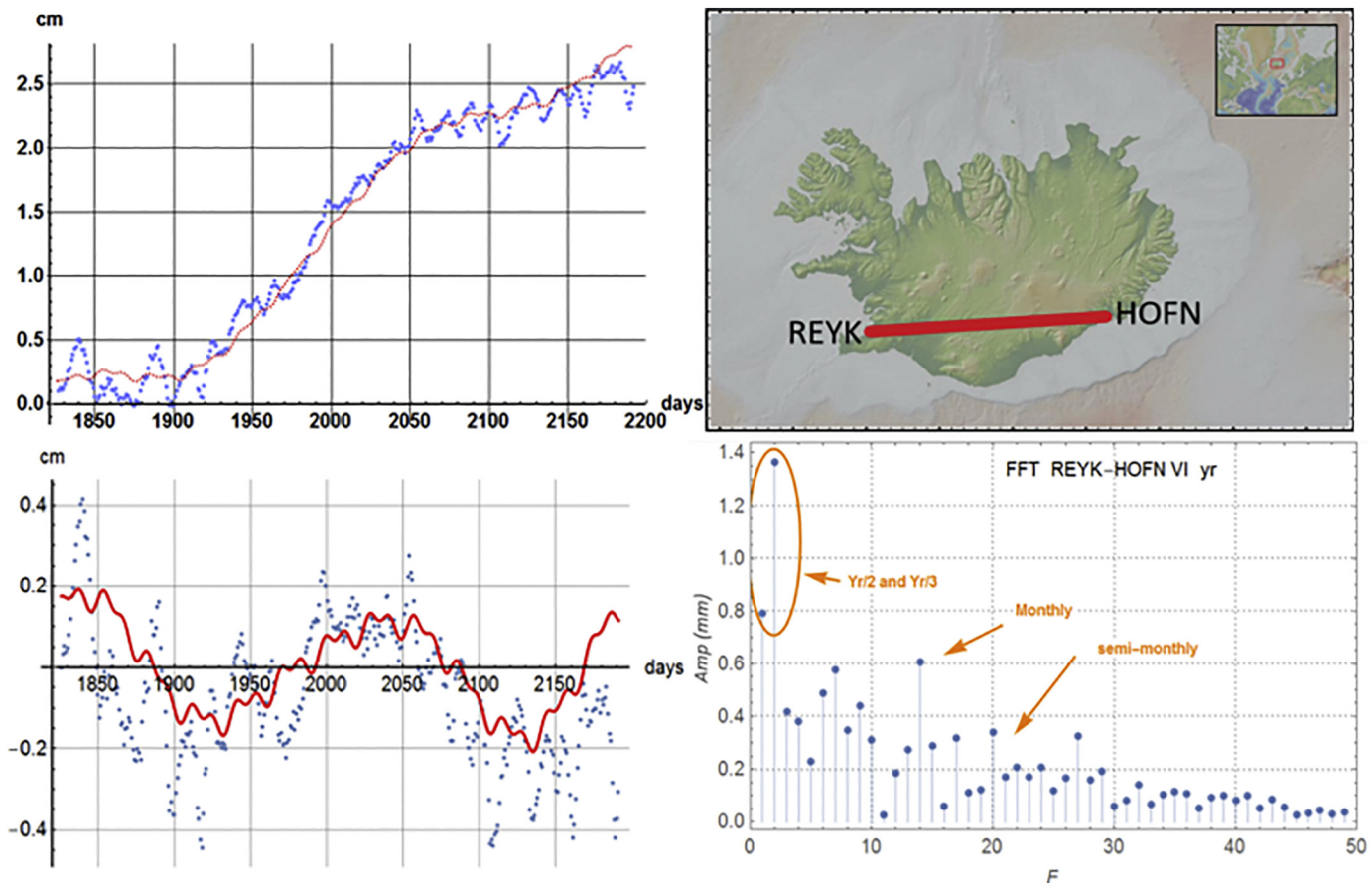


**Fig. 14.** Detail of the increasing distance among the two sites in Iceland across the Mid Atlantic Ridge in two separate years of the recorded data along the baseline. It is noteworthy to see how there is an about six months period in which the residuals increase, hence proving a faster lengthening.

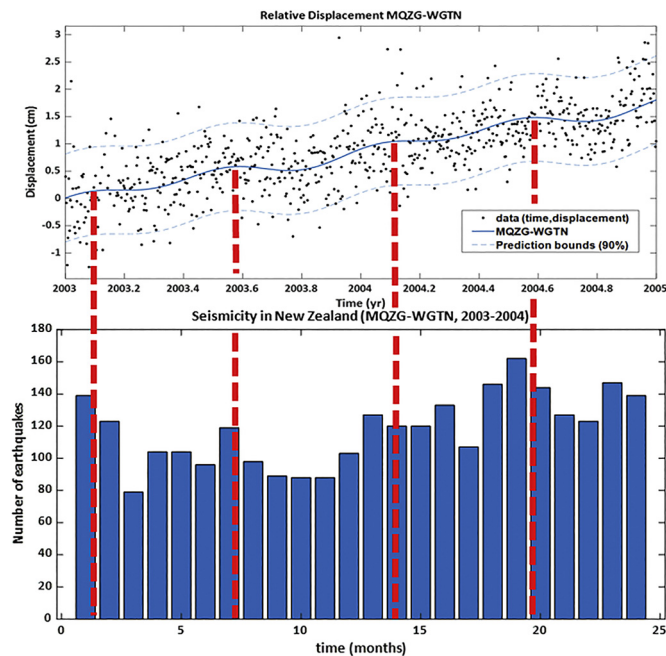


**Fig. 15.** Displacement recorded by GNSS along the baseline MQZG-WGTN McQueens Valley-Wellington Airport (above) versus the number of earthquakes in New Zealand (below). Oscillations fit the tidal harmonics.

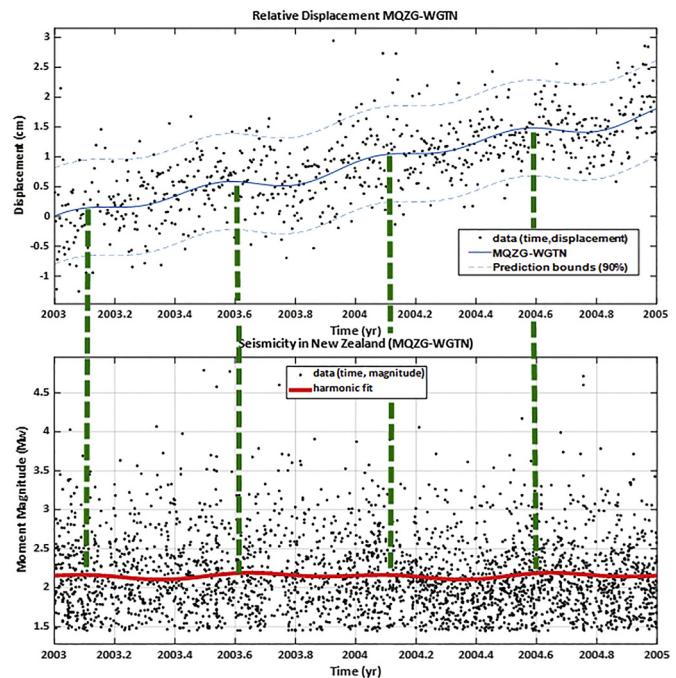


**Fig. 16.** Displacement recorded by GNSS along the baseline MQZG-WGTN (above) versus the magnitude of earthquakes in New Zealand (below). Oscillations fit the tidal harmonics.

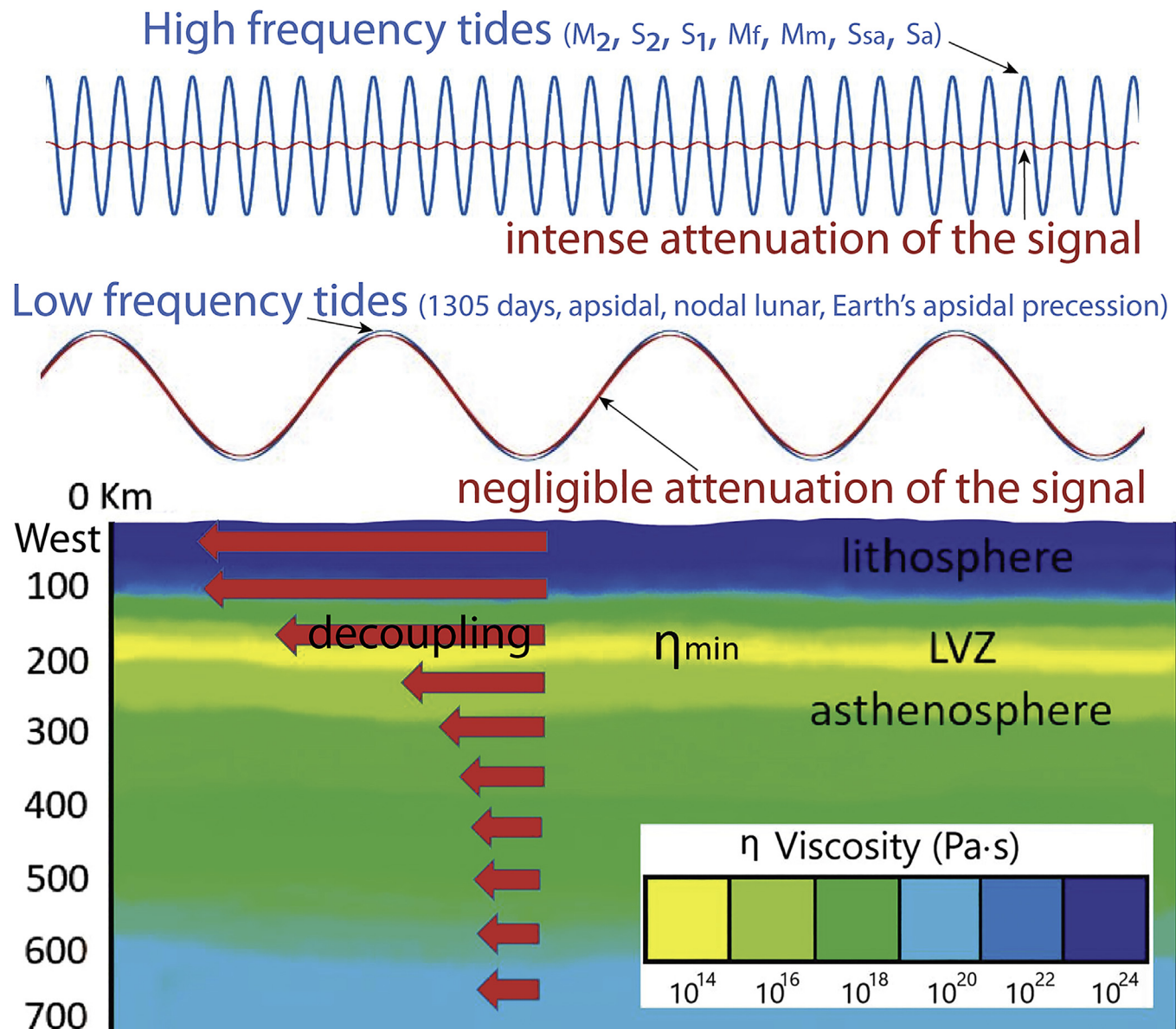


**Fig. 17.** The high-frequency tidal oscillations are buffered by the high viscosity of the lithosphere and upper mantle. However, the low-frequency tidal modulations are rather poorly attenuated by the lithosphere and mantle and therefore they may be very effective on the Earth. Although the average high viscosity value of the upper mantle, the presence of the low-velocity zone (LVZ) at 100–200 Km depth atop the asthenosphere, makes it possible to westerly decouple the lithosphere from the underlying mantle under the action of low frequency lunisolar tidal forces. This can be due to the lower viscosity and shorter Maxwell time of the LVZ. Notice that the amplitudes of the of 18.6, 9.3, 8.85 and 1305 years-long period harmonics are substantially well proportioned in their amplitude, moreover, the annual solar tide is attenuated, while the six-month or higher frequency harmonics are weak. This result does not change either by minimizing noise or carefully choosing the baseline to optimize the observation capacity of the higher frequency harmonics. The low-velocity zone behaves like a low-pass filter attenuating the high-frequency harmonics (for instance  $M_2, S_2, S_1, M_f, M_m, S_{sa}, S_a$ ), being its viscosity value still too high; hence the LVZ has an almost fully elastic behaviour. Decreasing the frequency, the elastic response disappears while the visco-plastic response increases (1305 days long-period harmonic, 4.4, 8.85, 9.3, 18.61, 25,772 years-long tides).

#### 4. Tidal harmonics versus seismicity

The correlation between lunisolar tides and earthquakes has been highly debated during the last decades, showing pros (Heaton, 1975; Métivier et al., 2009) and cons (Vidale et al., 1998; Hough, 2018). Usually, it has been considered the vertical influence of the tide and its modification of  $g$ . However, the vertical component of the tide returns to the origin point after the passage, whereas the horizontal component leaves the residual displacement. Therefore, the horizontal component of body tides is an ideal candidate to energize the tectonic system, whereas the vertical component is only modulating it, acting oppositely as a function of the tectonic setting (Riguzzi et al., 2010). Normal fault earthquakes occur more frequently during the low tide because  $g$  is at

its maximum and therefore the vertical  $\sigma_1$  is increased, enlarging the Mohr circle to the right. Vice versa, thrust-related earthquakes occur more frequently during the high tide because  $g$  is at its minimum and therefore the vertical  $\sigma_3$  is decreased, enlarging the Mohr circle to the left (see Fig. 10 in Riguzzi et al., 2010). If plates move faster during specific periods of the year due to the larger horizontal component of the body tide as it can be shown in the Iceland baseline (Fig. 14), we should expect more intense seismicity as well. The displacement recorded by GNSS along the baseline MQZG-WGTN McQueens Valley-Wellington Airport versus the number of earthquakes in New Zealand shows oscillations fitting the tidal harmonics of the horizontal component (Fig. 15). The same correlation holds for the comparison between the GNSS data and the magnitude momentum (Fig. 16). These

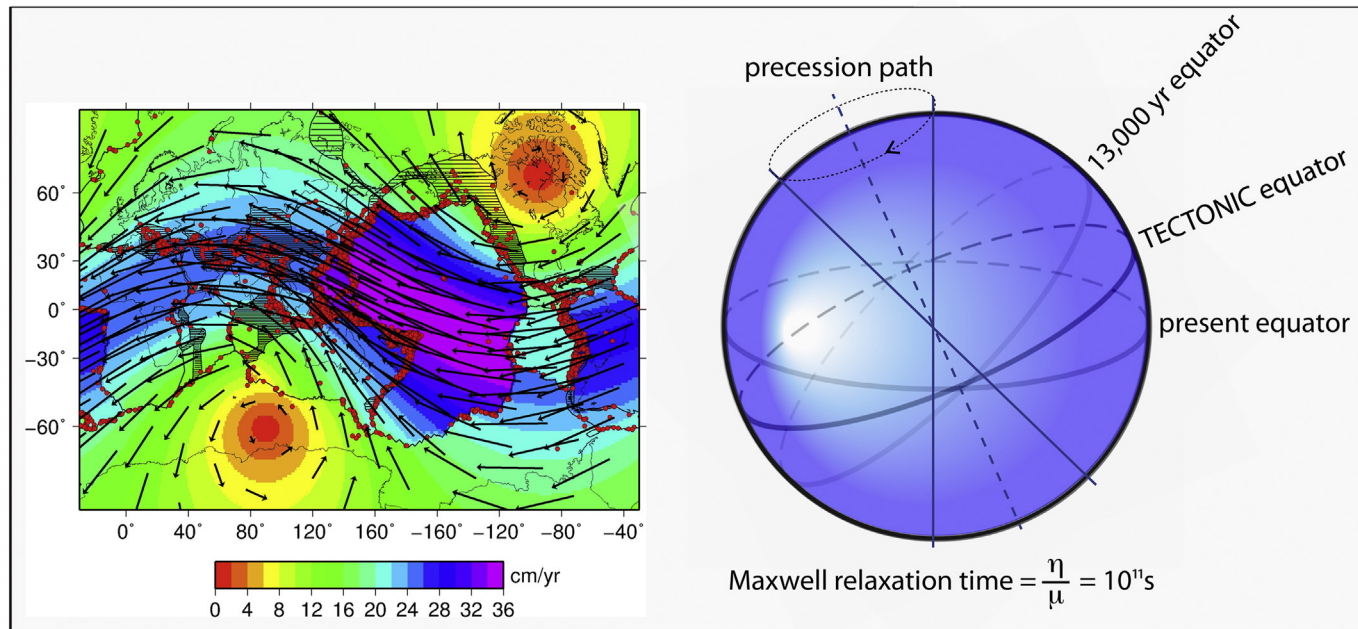


**Fig. 18.** Left, the mainstream of plate motions in the shallow hotspots reference frame (after Cuffaro and Doglioni, 2018). The red dots are earthquakes  $M \geq 6$  which disappear in the polar areas. The flow of plates and its tectonic equator have an inclination that is close to the ecliptic plane plus the Moon revolution plane (about  $29^\circ$ ) and it mimics the angle of the Moon projection on the Earth. Right, the tectonic equator represents the bisector of the present geographic equator and the equator inclination in 13,000 yr due to the Earth's axis precession. The Earth lithosphere has a Maxwell time (viscosity  $\eta/\mu$  rigidity) compatible with the precession time (26,000 yr), explaining a visco-plastic behaviour of the lithosphere at that timescale and the inclination of the tectonic versus the geographic equator. (For interpretation of the references to colour in this figure legend, the reader is referred to the web version of this article.)

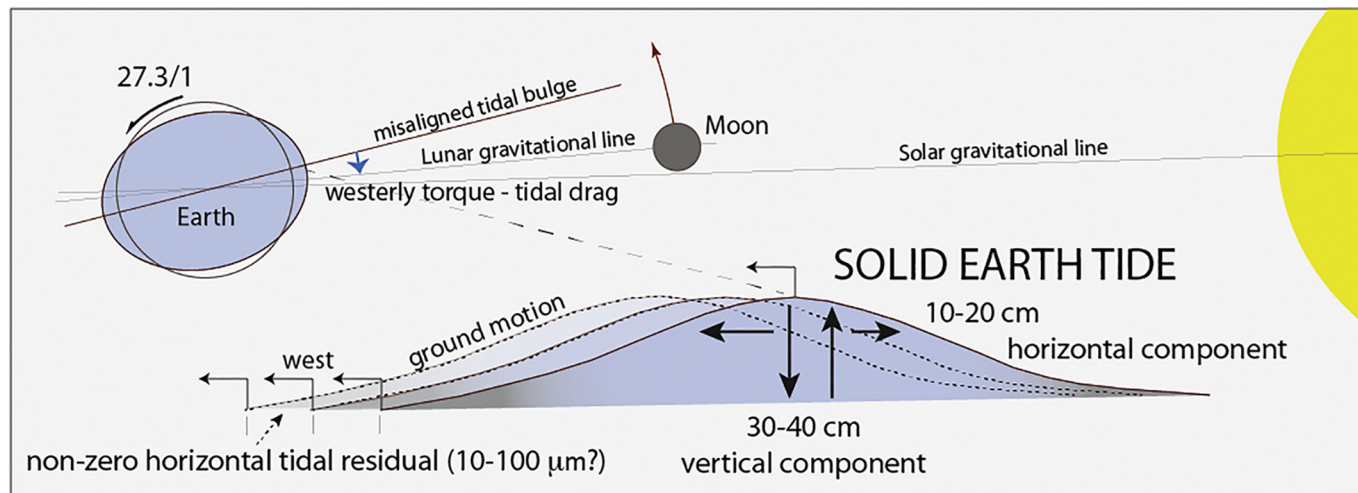


**Fig. 19.** Lunisolar tidal drag on the Earth. The Earth viewed from above the North pole rotates eastward about 28 times faster than the Moon and the tidal bulge is misaligned ( $\approx 0.1\text{--}0.3^\circ$ ) relative to the gravitational alignment among the two celestial bodies, due to the delay generated by the anelastic component of our planet. The misplaced excess of mass and the faster rotation determine a westerly-directed torque on the lithosphere that is tuned by the tidal harmonics, which leave a non-zero horizontal component of the tidal drag, controlling plate velocities. Notice the longer "westerly" vector of the horizontal displacement which determines the residual.

observations tell us that even the least energetic seismicity is affected by tides, not only the strongest. It suggests that the tides act through a double mechanism on the modulation of seismicity: the high-frequency harmonics (semi-diurnal, daily, monthly, half-yearly and annual) by triggering breaking processes in the brittle phase, while the low-frequency harmonics (apsidal and nodal precessions) modulate the mean energy release changing relative plates speed in the light of a plastic response of the asthenosphere and, overall, of the LVZ, which alters dynamic stability in the upper layers). Therefore, two different ideal regimes coexist in the Earth's surface response to the harmonic spectrum becoming clearly distinguished only in the limits of high and low

frequency, while they mix in the middle in different proportions, according to the frequency of the tidal harmonic.

## 5. Discussion and conclusions

Contrasting evidence has been provided on the effective contribution of the Moon and Sun on the driving mechanisms of lithospheric drift and the interplay with mantle convection. However, the tectonic asymmetries at plate boundaries, the westward drift of the lithosphere and the tectonic equator support a tidal contribution to plate tectonics (Doglioni and Panza, 2015; Cuffaro and Doglioni, 2018). Plate motions

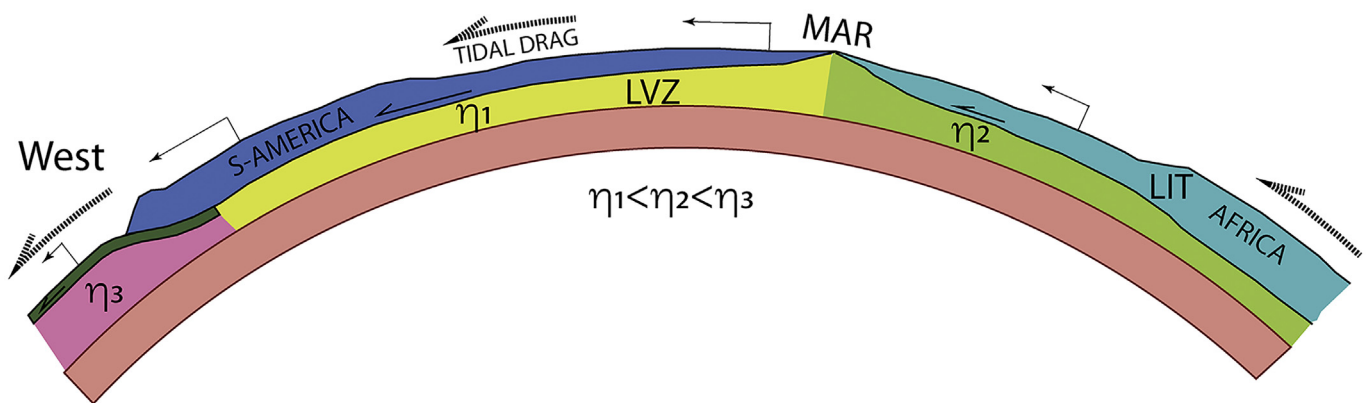


**Fig. 20.** The swinging body tides release a permanent residual accounting for the relative motion among tectonic plates as shown in the previous figures. Since the entire lithosphere (LIT) has a net westerly directed rotation, moving along the tectonic equator, the different velocity of plates can be inferred as related to the variable decoupling at the lithosphere base, dictated by the viscosity in the low-velocity zone (LVZ). The faster westerly motion of plates occurs where the underlying LVZ has the lowest viscosity ( $\eta_1$ ), and the slower has the higher viscosity ( $\eta_3$ ).

show a change in relative speed due to the action of the horizontal component of the lunisolar tides. Therefore, this phenomenon drags and modulates the shift of the lithosphere with respect to the underlying mantle. The high-frequency tidal oscillations are buffered by the high viscosity of the lithosphere and upper mantle. However, the low-frequency tidal oscillations are rather poorly attenuated by the lithosphere and mantle and therefore they may be very effective on the Earth due to a better correlation of their amplitude with the relaxation time of the lithosphere and mantle (Fig. 17). It is interesting to note that the strongest signal is given by the nutation of the Earth's axis. Moreover, the precession of nodes mimics the oscillations of the length of the day (LOD) that has some correlation with seismicity (Riguzzi et al., 2010). Seismicity is not instantaneously affected by the action of external forces, explaining the weak correlation between earthquakes and Moon position (Tanaka et al., 2002; Beeler and Lockner, 2003). On the other hand, there is statistical evidence of some relation for crustal faults and earthquakes (see an up-to-date discussion by Kossobokov and Panza, 2020) during the high tide for thrusts (Cochran et al., 2004; Métivier et al., 2009) and during the low tide for normal faults (Wilcock, 2001; Tolstoy et al., 2002; Riguzzi et al., 2010), coherent with the opposite contribution of the lithostatic load in the two different tectonic settings. The vertical component of the solid Earth tide decreases (high tide) or increases (low tide) respectively the lithostatic load acting on the crustal volumes and, on the faults, thus favouring their activation with a bipolar signal. The horizontal tidal component appears a driving force of plate motions and the gradients of velocity among plates accumulate the energy source dissipated by earthquakes. If we assume 0.48 kPa of horizontal stress at the passage of the body tide (Varga and Grafarend, 2018) that could be at least partially elastically retained (10%?) in the crust, times 365 days  $\times$  twice a day  $\times$  300 years, it would result more than 10 MPa, which is in the order of a stress drop of a major earthquake. The vertical component of tides (both solid and liquid) may trigger seismicity only when the horizontal energy threshold is reached. The tidal vertical loading or unloading cannot be the energy source for earthquakes (Riguzzi et al., 2010).

Therefore, tides should accumulate the hysteresis of the horizontal component of the body tide. However, this is still difficult to detect because of the limited accuracy of the space geodesy data. For example, a baseline increasing at 3 cm/yr would generate a residual of the semidiurnal component of 40  $\mu\text{m}$  that are well below the uncertainty of the GNSS measurement. The measure of relative plate motions demonstrates at least two main cycles of velocity variation at 8.8 yr and the stronger 18.6 yr, being respectively the alignment of apsides and Moon's nodal precession. These data indicate a tidal frequency of plate speed that supports the influence of astronomical gravitational forces on plate velocity, which are consistent with the westerly directed drift

of the lithosphere and the related tectonic equator (Fig. 18), plus the worldwide asymmetric tectonics of plate boundaries (Doglioni and Panza, 2015 and references therein).

Global relative plate motions are usually computed under the assumption of a no-net-rotation reference frame (Argus et al., 2011). However, plate motions measured in the hotspot reference frame rather highlight a net westerly-directed rotation of the lithosphere with respect to the underlying mantle (Crespi et al., 2007). The origin and speed of the net rotation of the lithosphere depend on the interpretation whether magmatic hotspots are fed by the deep mantle or they are rather shallow sources (Doglioni et al., 2005; Cuffaro and Doglioni, 2007; Foulger and Jurdy, 2007; Foulger, 2010). The deep mantle hotspot reference frame being a supports a slow (0.1°/Myr) transient and ephemeral effect on plate tectonics during the last 150 Myr due to variable negative buoyancy along W-directed subduction zones (Torsvik et al., 2010). The shallow mantle hotspot reference frame rather supports a faster (> 1°/Myr) permanent mechanism of astronomical origin for the net 'westerly' directed lithospheric rotation (Crespi et al., 2007; Doglioni et al., 2011; Doglioni and Panza, 2015). The shallow hotspot reference frame is consistent with the global rotation and the distributed tectonic asymmetries worldwide, such as the steeper W-directed slab, low elevation accretionary prism and occurrence of a backarc basin, deep trenches and foredeep basins in contrast with the opposite E- or NE-directed subduction zones which are characterized by shallow dip slabs, elevated mountain range composed by deep-seated rocks, shallow foredeeps and no backarc basin. Asymmetries among the flanks of oceanic rifts have been also recognized, such as shallower bathymetry, slower shear waves velocity and possibly depleted asthenosphere in the eastern side (Doglioni et al., 2003; Panza et al., 2010; Chalot-Prat et al., 2017). Therefore, we conclude that the horizontal component of the lunisolar tides contributes to driving tectonic plates (Fig. 19). Low-frequency tidal oscillations are compatible with the resonance time of the lithosphere and can drag plates over the asthenospheric mantle. This explains the faster semiannual oscillations of plate velocity that correlate with more intense seismicity. The horizontal gravitational swinging back and forth of plates due to the asymmetric body tide leaves a residual motion to the 'west'. Variable decoupling at the lithosphere base due to chemical and viscosity variations in the low-velocity zones determine fragments of the lithosphere (i.e., plates) moving with different velocity, hence providing plate tectonics (Fig. 20). The Earth's is slowing its spinning of about 2 ms/century and the Moon is receding 3.8 cm/yr. We also know that in the early Paleozoic the year was about 400 days and the day about 21 h long (Varga, 2006). It is easy to infer that in the past when the Moon was much closer and the Earth rotating faster. Therefore, the tidal effects and plate motions should have been larger and faster in the past.

Since the tidal drag is confirming the westerly directed motion of the lithosphere relative to the mantle ( Crespi et al., 2007 ), this observation claims for an Earth where the different layers have variable Maxwell time, different velocity and possibly each sphere being rotating independently and faster-moving down to the inner core that is spinning eastward faster than the outer layers ( Zhang et al., 2005 ). Due to the variable rheology of the internal layers of the planet, the astronomical torques make the Earth as a sort of gyroscope.

## Acknowledgements

The article benefited from the constructive reading of anonymous reviewers, Fernando Sansò and Peter Varga. Thanks for the useful discussions during the years to Don Anderson, Michael Bevis, Dino Boccaletti, Antonio Carcatera, Eugenio Carminati, Françoise Chalot-Prat, Mattia Crespi, Marco Cuffaro, Giorgio Vittorio Dal Piaz, Eleonora Ficini, Eduardo Garzanti, Giuliano Panza, A. Ismail-Zadeh, Enzo Nesi, Fulvio Ricci, Benedetto Scoppola and Federica Riguzzi. The maps included in the figures were made with GeoMapApp ([www.geomapapp.org/](http://www.geomapapp.org/)) / CC BY / (Ryan et al., 2009).

## Declaration of Competing Interest

The authors declare that they have no known competing financial interests or personal relationships that could have appeared to influence the work reported in this paper.

## References

- Afonso, J.C., Ranalli, G., Fernandez, M., 2007. Density structure and buoyancy of the oceanic lithosphere revisited. *Geophys. Res. Lett.* 34 (10), L10302.
- Agnew, D.C., 2007. Earth Tides. University of California 174.
- Altamimi, Z., Rebischung, P., Métivier, L., Collilieux, X., 2016. ITRF2014: A new release of the International Terrestrial Reference Frame modeling nonlinear station motions. *J. Geophys. Res. Solid Earth*, 121, doi: <https://doi.org/10.1002/2016JB013098>
- Anderson, D.L., Natland, J.H., 2014. Mantle updrifts and mechanisms of oceanic volcanism. *Proc. Natl. Acad. Sci.* 111 (41), E4298 –E4304.
- Argus, D.F., Gordon, R.G., 1991. No-net-rotation model of current plate velocities incorporating plate motion model NUVEL-1. *Res. Lett.* 1991, 2039 –2042 (ISSN 0094-8276), vol. 18, Nov .
- Argus, D.F., Gordon, R.G., DeMets, C., 2011. Geologically current motion of 56 plates relative to the no-net-rotation reference frame. *Geochem. Geophys. Geosyst.* 12 (11). <https://doi.org/10.1029/2011GC003751>
- Argus, D.F., Fu, Y., Landauer, F.W., 2014. Seasonal variation in total water storage in California inferred from GPS observations of vertical land motion. *Geophys. Res. Lett.* 41, 1971 –1980. <https://doi.org/10.1002/2014GL059570>
- Bak, P., Tang, C., 1989. Earthquakes as a Self-Organized critical Phenomenon. *J. Geophys. Res.* 84 (B1) 635 –15, (637) .
- Bates, D.M., Watts, D.G., 1988. Nonlinear Regression Analysis and its Applications. Wiley
- Beeler, N.M., Lockner, D.A., 2003. Why earthquakes correlate weakly with the solid Earth tides: Effects of periodic stress on the rate and probability of earthquake occurrence. *J. Geophys. Res.* 108, B8 .
- Blewitt, G., Hammond, W.C., Kreemer, C., 2018. Harnessing the GPS Data explosion for interdisciplinary science. *Eos* 99 .
- Bostrom, R.C., 1971. Westward displacement of the lithosphere. *Nature* 234, 536 –538.
- Carcatera, A., Doglioni, C., 2018. The westward drift of the lithosphere: a tidal ratchet? *Geosci. Front.* 9 (2), 403 –414. <https://doi.org/10.1016/j.gsf.2017.11.009>
- Cartwright, D.E., Edden, A., 1973. Corrected Tables of Tidal Harmonics. *Geophys. J. Royal Soc.* 33, 253 –264.
- Cathles, L.M., 1975. The Viscosity of the Earth's Mantle. Princeton, Princeton University Press 386 p.
- Chalot-Prat, F., Doglioni, C., Falloon, T., 2017. Westward migration of oceanic ridges and related asymmetric upper mantle differentiation. *Lithos* 268 –271, 163 –173. <https://doi.org/10.1016/j.lithos.2016.10.036>
- Cochran, E.S., Vidale, J.E., Tanaka, S., 2004. Earth tides can trigger shallow thrust fault earthquakes. *Science* 306 (5699), 1164 –1166.
- Crespi, M., Cuffaro, M., Doglioni, C., Giannone, F., Riguzzi, F., 2007. Space geodesy validation of the global lithospheric flow. *Geophys. J. Int.* 168, 491 –506. <https://doi.org/10.1111/j.1365-246X.2006.03226.x>
- Cuffaro, M., Doglioni, C., 2007. Global Kinematics in the deep versus shallow hotspot reference frames. In: Foulger, G.R., Jurdy, D.M. (Eds.), *Plates, Plumes, and Planetary Processes*. 430. pp. 359 –374. [https://doi.org/10.1130/2007.2430\(18\).Geo.Soc.Am.Spec.Pap](https://doi.org/10.1130/2007.2430(18).Geo.Soc.Am.Spec.Pap).
- Cuffaro, M., Doglioni, C., 2018. On the increasing size of the orogens moving from the Alps to the Himalayas in the frame of the net rotation of the lithosphere. *Gondwana Research* 62, 2 –13. <https://doi.org/10.1016/j.gr.2017.09.008>
- Dach, R., Lutz, S., Walser, P., Fridez, P., 2015. Bernese GNSS Software Version 5.2. User Manual. Astronomical Institute, University of Bern, Bern Open Publishing <https://doi.org/10.7892/boris.72297>. ISBN: 978-3-906813-05-9.
- Doglioni, C., 1993. Geological evidence for a global tectonic polarity. *J. Geol. Soc. Lond.* 150, 991 –1002.
- Doglioni, C., 1994. Foredeeps versus subduction zones. *Geology* 22 (3), 271 –274.
- Doglioni, C., Panza, G.F., 2015. Polarized plate tectonics. *Adv. Geophys.* 56 (3), 1 –167. <https://doi.org/10.1016/bs.agph.2014.12.001>
- Doglioni, C., Carminati, E., Bonatti, E., 2003. Rift asymmetry and continental uplift. *Tectonics* 22 (3), 1024. <https://doi.org/10.1029/2002TC001459>
- Doglioni, C., Green, D., Mongelli, F., 2005. On the shallow origin of hotspots and the westward drift of the lithosphere. In: Foulger, G.R., Natland, J.H., Presnall, D.C., Anderson, D.L. (Eds.), *Plates, Plumes and Paradigms*. 388. pp. 735 –749 Geological Society of America Sp. Paper .
- Doglioni, C., Carminati, E., Cuffaro, M., Scrocca, D., 2007. Subduction kinematics and dynamic constraints. *Earth-Sci. Rev.* 83, 125 –175.
- Doglioni, C., Ismail-Zadeh, A., Panza, G., Riguzzi, F., 2011. Lithosphere-asthenosphere viscosity contrast and decoupling. *Phys. Earth Planet. Inter.* 189, 1 –8.
- Ficini, E., Dal Zilio, L., Doglioni, C., Gerya, T., 2017. Horizontal mantle flow controls subduction dynamics. *Sci. Rep.* 7, 7550. <https://doi.org/10.1038/s41598-017-06551-y>
- Ficini, E., Cuffaro, M., Doglioni, C., 2020. Asymmetric Dynamics at Subduction zones Derived from Plate Kinematic Constraints. *Gondwana Res.* 78, 110 –125. <https://doi.org/10.1016/j.gr.2019.07.013>
- Foulger, G.R., 2010. *Plates vs. Plumes: A Geological Controversy*. Wiley-Blackwell, pp. 2010 364 p, ISBN 978-1-4051-6148-0
- Foulger, G.R., Jurdy, D.M. (Eds.), 2007. *Plates, Plumes, and Planetary Processes*, Geological Society of America Sp. Paper, 430 .
- Fu, Y., Freymueller, J.T., 2012. Seasonal and long-term vertical deformation in the Nepal Himalaya constrained by GPS and GRACE measurements. *J. Geophys. Res.* 117 (B3) GeoNet Earthquake Catalogue for New Zealand, 2020.
- Gradstein, F.M., Ogg, J.G., Schmitz, M., Ogg, G. (Eds.), 2012. *The Geologic Time Scale 2012*. Elsevier 1114 p .
- Heaton, T.H., 1975. Tidal triggering of Earthquakes. *Geophys. J. Int.* 43 (2), 307 –326.
- Hough, S.E., 2018. Do large (magnitude  $\geq 8$ ) global earthquakes occur on preferred days of the calendar year or lunar cycle? *Seismol. Res. Lett.* 89 (2A), 577 –581. <https://doi.org/10.1785/0220170154>
- Hu, Y., Bürgmann, R., Banerjee, P., Feng, L., Hill, E.M., Ito, T., Tabei, T., Kelin Wang, K., 2016. Asthenosphere rheology inferred from observations of the 2012 Indian Ocean earthquake. *Nature* 538 .
- Jin, Z.-M., Green, H.G., Zhou, Y., 1994. Melt topology in partially molten mantle peridotite during ductile deformation. *Nature* 372, 164 –167.
- Jordan, T.H., 1974. Some comments on tidal drag as a mechanism for driving plate motions. *J. Geophys. Res.* 79 (14), 2141 –2142.
- Knopoff, L., Leeds, A., 1972. Lithospheric momenta and the deceleration of the Earth. *Nature* 237 (12), 93 –95.
- Kossobokov, V.G., Panza, G.F., 2020. A myth of preferred days of strong earthquakes? *Seismol. Res. Lett.* XX, 1 –8. <https://doi.org/10.1785/0220190157>
- Kudryavtsev, S., 2004. Improved harmonic development of the Earth tide-generating potential. *J. Geod.* 77, 829 –838.
- Le Pichon, X., 1968. Sea- floor spreading and continental drift. *J. Geophys. Res.* 73 (12), 3661 –3697.
- Lowrie, W., 2007. *Fundamentals of Geophysics*. Cambridge University Press
- MacDonald, G.J., 1964. Tidal friction. *Rev. Geophys.* 2, 467 –541.
- Mei, S., Bai, W., Hiraga, T., Kohlstedt, D.L., 2002. Influence of Melt on the Creep Behaviour of Olivine Basalt Aggregates under Hydrous Conditions: Earth and Planetary Science Letters. 201. pp. 491 –507. [https://doi.org/10.1016/S0012-821X\(02\)00745-8](https://doi.org/10.1016/S0012-821X(02)00745-8)
- Métivier, L., de Viron, O., Conrad, C.P., Renault, S., Diamant, M., Patau, G., 2009. Evidence of earthquake triggering by the solid earth tides. *Earth Planet. Sci. Lett.* 278 (3–4), 370 –375.
- Moore, G.W., 1973. Westward tidal lag as the driving force of plate tectonics. *Geology* 1, 99 –100. <https://doi.org/10.1130/0091-7613>
- Munk, W., 1997. Once again: once again tidal friction. *Prog. Oceanogr.* 40, 7 –35.
- Munk, W.H., McDonald, G.J.F., 1960. *The Rotation of the Earth: A Geophysical Discussion*. Cambridge University Press, Cambridge 323 p .
- Nasa, 2020. *HORIZONS Lunar and Solar Ephemerides 2020*. Jet Propulsion Laboratory. <https://ssd.jpl.nasa.gov/horizons.cgi#top>
- Nelson, T.H., Temple, P.G., 1972. Mainstream Mantle Convection; A Geologic Analysis of Plate Motion. 56. *American Association of Petroleum Geologists Bulletin*, pp. 226 –246 .
- Panza, G., Doglioni, C., Levshin, A., 2010. Asymmetric Ocean basins. *Geology* 38 (1), 59 –62. <https://doi.org/10.1130/G30570.1>
- Pollitz, F.F., Bürgmann, R., Romanowicz, B., 1998. Viscosity of oceanic asthenosphere inferred from remote triggering of earthquakes. *Science* 280, 1245 –1249. <https://doi.org/10.1126/science.280.5367.1245>
- Riguzzi, F., Panza, G., Varga, P., Doglioni, C., 2010. Can Earth's rotation and tidal de-spinning drive plate tectonics? *Tectonophysics* 484, 60 –73. <https://doi.org/10.1016/j.tecto.2009.06.012>
- Ryan, W.B.F., Carbotte, S.M., Coplan, J.O., O'Hara, S., Melkonian, A., Arko, R., Weissel, R.A., Ferrini, V., Goodwillie, A., Nitsche, F., Bonczkowski, J., Zemsky, R., 2009. Global Multi-Resolution Topography synthesis. *Geochim. Geophys. Geosyst.* 10, Q03014. <https://doi.org/10.1029/2008GC002332>
- Sabadini, R., Lambeck, K., Boschi, E., 1991. *Glacial Isostasy, Sea Level and Mantle Rheology*. Springer .
- Scoppola, B., Boccaletti, D., Bevis, M., Carminati, E., Doglioni, C., 2006. The westward drift of the lithosphere: a rotational drag? *Bull. Geol. Soc. Am.* 118, 199 –209. <https://doi.org/10.1130/B25734.1>
- Shen, W., Nab, S.H., 2017. Atmospheric acceleration and Earth-expansion deceleration of

- the Earth rotation. *Geodesy Geodyn.* 8 (6), 421–426. <https://doi.org/10.1016/j.geog.2017.02.002>.
- Smith, S.W., Jungels, P., 1970. Phase delay of the solid earth tide. *Phys. Earth Planet. Inter.* 2 (4), 233–238.
- Tanaka, S., Ohtake, M., Sato, H., 2002. Evidence for tidal triggering of earthquakes as revealed from statistical analysis of global data. *J. Geophys. Res.* 107 (B10), 2211.
- Tolstoy, M., Vernon, F.L., Orcutt, J.A., Wyatt, F.K., 2002. Breathing of the seafloor: tidal correlations of seismicity at Axial volcano. *Geology* 30 (6), 503–506.
- Torsvik, T.H., Steinberger, B., Gurnis, M., Gaina, C., 2010. Plate tectonics and net lithosphere rotation over the past 150 my. *Earth Planet. Sci. Lett.* 291 (1–4), 106–112.
- Tregoning, P., van Dam, T., 2005. Atmospheric pressure loading corrections applied to GPS data at the observation level. *Geophys. Res. Lett.* 32 (22).
- United States Geological Survey, 2020. Earthquake Catalog, USGS. <https://earthquake.usgs.gov/earthquakes/eventpage>.
- Varga, P., 2006. Temporal variation of geodynamical properties due to tidal friction. *J. Geodyn.* 41, 140–146.
- Varga, P., Grafarend, E., 2018. Influence of tidal forces on the triggering of seismic events. *Pure Appl. Geophys.* 175 (5), 1649–1657. <https://doi.org/10.1007/s00024-017-1563-5>.
- Varga, P., Denis, C., Varga, T., 1998. Tidal friction and its consequences in paleogeodesy, in the gravity field variations and in tectonics. *J. Geodyn.* 25, 61–84.
- Vespe, F., Rutigliano, P., Ferraro, C., Nardi, A., 2002. Vertical reference systems. Cartagena (Colombia). IAG Simposia 124, 66–71.
- Vespe, F., Rutigliano, P., Pacione, R., 2003. The Treatment of Time Series Data of GPS Permanent Stations for Extracting Geodetic Signals. In: Proc. of the Bilateral Geodetic Meeting Italy-Poland, Reports on Geodesy, pp. 53–64.
- Wahr, J., 1995. Global Earth Physics. 1. pp. 40–46.
- Wilcock, W.S.D., 2001. Tidal triggering of microearthquakes on the Juan de Fuca Ridge. *Geophys. Res. Lett.* 28 (20), 3999–4002.
- Zhang, J., Song, X., Li, Y., Richards, P.G., Sun, X., Waldhauser, F., 2005. Inner Core Differential Motion Confirmed by Earthquake Waveform Doublets. *Science* 309 (5739), 1357–1360.